



On the dynamics and air-quality impact of the exceptional East Asian dust outbreak in mid-March 2021

Feifei Mu^{1,*}, Eduardo Weide Luiz, Stephanie Fiedler^{1,2}

University of Cologne, Institute of Geophysics and Meteorology, Pohligstr. 3, Cologne 50969, Germany

ARTICLE INFO

Keywords:

Mongolian cyclone
Nocturnal low-level jet
Dust storm
Gobi Desert
Taklamakan Desert

ABSTRACT

In mid-March 2021, one of the strongest dust storms of the last decade hit East Asia with adverse impacts on socio-economic activities and loss of life. The aim of this study is to assess the atmospheric dynamics involved in the temporal evolution of the Mongolian extra-tropical cyclone driving the dust event in different dust source regions in East Asia and to quantify to what extent the event was unusual for the first time. To that end, we use observation and model data from different sources. We identify that dust aerosols of the event primarily originated in the Gobi Desert. The anomalously strong dust-emitting winds were here associated with the passage of a cold front and exceeded the 99th percentile of the near-surface wind climatology for March 1992–2021 by far. Over the Loess Plateau, the dust deposition mostly exceeded the regional dust emission, indicative of the region being a net sink for dust aerosols, even during a high-impact event like in mid-March 2021. The formed dust aerosol layer of thousands of kilometers in extent led to sharp decreases in the air quality across China with record-high urban particulate matter concentrations, poor air quality, and low atmospheric visibility. Our results highlight that also the Taklamakan Desert contributed to the dust outbreak in the Western part of China. The dust emissions in the Taklamakan Desert were associated with nocturnal low-level jets that were favored by the cold air intrusion. It provides the first evidence for a link between different dust-emission mechanisms across East Asian Deserts during synoptic-scale dust outbreaks.

1. Introduction

East Asia witnessed a high-impact dust storm on 13–16 March 2021. The dust storm took lives and destroyed houses across Mongolia. In China, the dust outbreak affected an area of more than 3.8 million square kilometers and resulted in the cancellations of public transportation and outdoor activities in many cities. The arid and semiarid areas in East Asia, such as the Taklamakan Desert and the Gobi Desert, are known as active dust sources (Bian et al., 2011; Ge et al., 2014; Song et al., 2016; Chen et al., 2017). The large desert area paired with the relatively frequent dust-emitting winds makes the Taklamakan Desert the most active dust source region in East Asia (Wang et al., 2015). Generally, dust emissions in the Taklamakan Desert are particularly large during the Northern hemisphere spring and summer (Ge et al., 2014). During the years 2007 to 2011, the mean spring and summer dust emissions in the Taklamakan Desert were 70.5 Tg yr^{-1} and 58.8 Tg yr^{-1} , contributing 39% and 42% of the total annual dust emission of East Asia

(Chen et al., 2017).

Compared to the Taklamakan Desert, dust source activation in the Gobi Desert is less frequent (Tao et al., 2022). However, the Gobi Desert is known as the source of severe dust outbreaks affecting East Asia (Bian et al., 2011). The dust emissions in northern East Asia are particularly active in spring due to the seasonality of the extra-tropical cyclones (Takemi and Seino, 2005; Cuesta et al., 2015; Tian et al., 2020). Owing to the relatively high elevation and the typically low soil moisture, soil particles can here be mobilized when the wind speed is sufficiently strong (Kim and Choi, 2015; Chen et al., 2017). Additionally, the Chinese Loess Plateau is known for dust activity (Zhang et al., 2010; Feng and Wang, 2012; Guan et al., 2017). However, dust emissions there are typically lower than in the Taklamakan and the Gobi Desert, and most of the severe dust events reported for the Plateau are associated with advected dust-laden air from elsewhere (Huang et al., 2008).

Dust outbreaks from East Asia significantly contribute to the regional and global dust aerosol cycle, primarily in spring and summer (Kok

* Corresponding author.

E-mail addresses: feifei.mu@uni-koeln.de (F. Mu), eweidelu@uni-koeln.de (E.W. Luiz), sfiedler@geomar.de (S. Fiedler).

¹ Now at GEOMAR Helmholtz Centre for Ocean Research Kiel, Kiel, Germany.

² Now at Faculty for Mathematics and Natural Sciences, Kiel University, Kiel, Germany.

et al., 2021). Strong springtime dust outbreaks from the Gobi Desert may transport dust over long distances and impair urban air quality. During a springtime dust storm in 2007, for instance, dust from the Gobi Desert contributed 58% and 88% to the dust-aerosol concentrations in the two coastal metropolises Hongkong and Shanghai (Zhang et al., 2017). Furthermore, Zhang et al. (2018) calculated that 5.3 Tg of aeolian dust from the Gobi Desert in May 2017 was deposited across the North Pacific Ocean. They observed dust aerosols at heights of 2–8 km a.g.l. one week after the dust emissions occurred in East Asia, indicating deep vertical mixing of the dust-laden air. In summer, dust aerosols from the Taklamakan Desert are frequently transported southwards and can accumulate at the northern slopes of the Tibetan Plateau (Yuan et al., 2019). This is different in spring when dust aerosols from the Taklamakan Desert can be transported eastwards such that they reach the American continent. Takemura et al. (2002) indicated that 10–20% of East Asian dust seen around Japan reached North America. Dust from the Taklamakan and the Gobi Desert might follow different trans-Pacific paths. Trajectory analyses indicate that dust aerosols to the South of 50°N and to the North of 50°N arriving in North America mainly stem from the Taklamakan and the Gobi Desert, respectively (Yu et al., 2019).

Dust aerosols play an important role in the regional climate by affecting the atmospheric radiation transfer and cloud processes (Ling et al., 2014; Song et al., 2018). In East Asia, the dust direct radiative effects show a seasonal cycle with a maximum in spring coinciding with the maximum in the dust-aerosol burden (Chen et al., 2014). A dust event in April 2011 resulted in daily mean regional surface radiative effects of -21.1 Wm^{-2} and an atmospheric radiative effect of $+12.7 \text{ Wm}^{-2}$ over the Gobi Desert (Liu et al., 2016), implying that the dust aerosols caused surface cooling paired with atmospheric warming. Due to the advection of dust-laden air, such effects are not limited to the dust source regions (Han et al., 2012). Moreover, Asian dust aerosols act as ice nucleating particles and therefore have also an indirect effect on the radiation budget (Kawai et al., 2021).

In addition to its effects on climate, dust aerosols have profound impacts on human health. Inhaled dust particles can reach the bronchioles and are a health risk, especially for elderly people, young children, and people who suffer from chronic cardiopulmonary diseases (Sandstrom and Forsberg, 2008; Schweitzer et al., 2018). In Minqin, a northwest city of China, high atmospheric concentrations of particulate matter due to dust storms are further a cause of pulmonary tuberculosis outbreaks during spring (Wang et al., 2016). These are two of several adverse health impacts of dust underlining the need to understand the occurrence of dust and its impacts on air quality.

Dust aerosols can be mobilized by strong near-surface winds when they exceed the threshold friction velocity for dust emissions in the source region. Such dust-emitting winds are favored by different mechanisms in different dust source region (e.g., Bou Karam et al., 2008; Kaskaoutis et al., 2015; Hamidianpour et al., 2021). Extra-tropical cyclones, which form over Mongolia and move southeastwards, are a known driver for dust emission in the Gobi Desert leading to dust outbreaks in East Asia (Takemi and Seino, 2005; Shao and Dong, 2006; Zhang et al., 2018; Bueh et al., 2022). Furthermore, the breakdown of Nocturnal Low-Level Jets (NLLJs) has been reported as a mechanism for dust-emitting winds for different deserts (Fiedler et al., 2013; Alizadeh-Chooabari et al., 2014). Specifically, NLLJs are known to play a role as a dust-emitting mechanism in the Taklamakan Desert (Ge et al., 2016), but have not been assessed in the context of extra-tropical cyclones before.

Dust emissions depend on the threshold friction velocity which is determined by soil conditions, such as soil moisture, vegetation cover, and surface crust (e.g., Shao and Lu, 2000). Higher soil moisture can lead to higher cohesive forces between soil particles and thus increase the thresholds for dust emission (Kim and Choi, 2015). Soil moisture can also contribute to increasing the vegetation cover in dust source regions, reducing or preventing dust emissions (An et al., 2018). In the past two decades, increasing soil moisture and vegetation cover have been

reported to be a reason for the decline in dust activities in East Asia (Wu et al., 2022).

The exceptional dust event in mid-March 2021 had serious impacts in both Mongolia and China and is thus of great interest for diverse reasons (e.g., Filonchik, 2022; Gui et al., 2022; Qian et al., 2022; HHan and Guan and Gu, 2021). The Mongolian cyclone is visible as a cloud band marking the cold front on 15 March 2021 from the Moderate Resolution Imaging Spectroradiometer (MODIS; Kaufman et al., 2002) in Fig. 1a. The yellow-colored dust aerosols cover large parts of China and are partly masked by cloud cover. A first characterization of the event concerning the dust origin, transport, and meteorological drivers was given by Gui et al. (2022). However, the differences in the Mongolian cyclone-related dust emission mechanisms between the Gobi Desert and the Taklamakan Desert, their relative contributions to the dust outbreak, and the impact on urban air quality has not been jointly assessed before. Our study contributes to a better understanding of the physical basis and impacts of the dust outbreak in March 2021 and quantitatively assesses to what extent the case was unusual. Specifically, the aims of our study are to give a first assessment of the atmospheric dynamics involved in the evolution of the dust outbreak, to evaluate to what extent the event was unusual from a climatological perspective, and to quantify the impact of the dust outbreak on urban air quality in China. We assess the relative contributions of dust from the Loess Plateau, the Taklamakan, and the Gobi Desert, motivated by the fact that their contributions strongly differed during past dust events in spring (Chen et al., 2017; Yu et al., 2019). To that end, we use seven data sets including large networks of ground-based observations from China, satellite images, and output from three different reanalyses (Section 2). The results are presented in chronological order of the meteorological development and the associated impacts on air quality (Section 3). We end with a discussion and conclusion from the analysis and give recommendations for future research (Section 4).

2. Data and methods

2.1. Observational data

We used four observational data sets for our study. The first one was the true color images from the satellite-based Moderate Resolution Imaging Spectroradiometer (MODIS). The MODIS sensor was launched on board both Terra and Aqua satellites and measures radiation in 36 different spectral bands (Kaufman et al., 2002). The MODIS true color images provide a picture of clouds and dust aerosols. Fig. 1a shows one of these images taken during the morning hours (around 10:30 BJT) on 15th March 2021 to give an overview of the horizontal characteristics of the dust outbreak.

Hourly data for atmospheric pollutants were taken from the China National Environmental Monitoring Centre (CNEMC). This dataset is available from December 2013 to the present from the Air Quality Online Monitoring and Analysis Platform. It currently collects atmospheric pollutants in a total of 367 cities in China, including Particulate Matter ($\text{PM}_{2.5}$ and PM_{10}), SO_2 , NO_2 , O_3 , CO , and reports the Air Quality Index (AQI). Based on the Chinese Ambient Air Quality Standards (CAAQS), AQI is calculated from the six pollutants SO_2 , NO_2 , CO , O_3 , $\text{PM}_{2.5}$, and PM_{10} . The values of AQI range from 0 to 500, and serious health effects are expected when AQI exceeds a value of 300 (Hu et al., 2015). We used this data in two ways. Firstly, we calculated the daily averaged PM_{10} concentrations during the dust event at all Chinese stations for all days with more than 16 h of valid data, similar to previous studies (e.g., Li et al., 2021; Li et al., 2022). The stations where the daily averaged PM_{10} exceeding the level for Grade II of the National Ambient Air Quality Standard in China ($150 \mu\text{g m}^{-3}$; MEP, 2012) were then used for illustrating the spatio-temporal impacts of the dust event assessed here. Secondly, the time series of the observed $\text{PM}_{2.5}$, PM_{10} , and AQI for six cities were selected for a more detailed assessment of the spatio-temporal development of the impacts on cities during the event (red

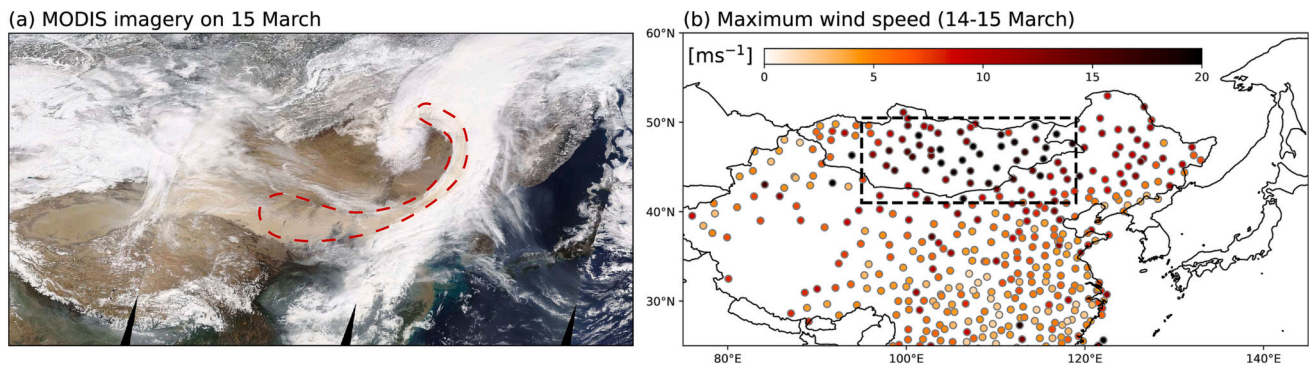


Fig. 1. Overview of the dust storm. Shown are (a) MODIS Terra visible imagery with the dust aerosols marked by a circle on 15 March 2021 over East Asia, and (b) maximum wind speeds at 10 m a.g.l. for 14–15 March 2021 with high dust-emitting winds area marked by the black dashed box in the Gobi Desert. The image in (a) is taken from NASA Worldview and clouds obscure parts of the dust aerosols during the event. Wind speed data in (b) are from meteorological station observations in China and Mongolia (see Methods section for details).

dots in Fig. 2a). The six cities are situated in the high-impact region of this event (black dashed box in Fig. 4f). The cities Zhangye, Lanzhou, Baotou, Yuncheng, Langfang, and Jinan, were selected for their geographical position that gives us an array of three times two stations along similar latitudes and longitudes.

We further obtained meteorological data from station observations from the US National Climatic Data Center (NCDC). Here, we used 3-hourly visibility data in March of the past 30 years (1992–2021). Since the visibility observation changed from manual to automatic in 2013, recordings before 2013 were corrected by multiplying the data with the factor 0.766, as in earlier works (Pei et al., 2018; Li et al., 2022). For each March, all stations with more than 80% valid data were selected for our analysis. The minimum visibility at each station was determined during times when the recorded wind speed exceeded 3 ms^{-1} and the relative humidity was less than 80%. These two criteria

excluded other phenomena that reduce atmospheric visibility, e.g., fog, haze, and rain (Li et al., 2022). We further use data from NCDC for the near-surface wind speed and the equivalent potential temperature (θ_e) at stations close to the six selected CNEMC stations that monitor the air quality. An increase in horizontal wind speed paired with a sharp gradient in potential temperature (θ) and equivalent potential temperature (θ_e) is used to identify the passage of the cold front, as also used in other studies (Abdi Vishkaee et al., 2012; Hamzeh et al., 2021). We further computed the maximum near-surface wind speeds for 14–15 March 2021 over Mongolia and China to illustrate the effects of the Mongolian cyclone on generating dust-emitting peak winds.

Moreover, we used the radiosonde data from four stations (black dots in Fig. 2a) in the Gobi and the Taklamakan Desert. Sounding balloons are launched at 08 BJT and 20 BJT to measure vertical profiles of the air temperature, wind speed and direction, and relative humidity. This data

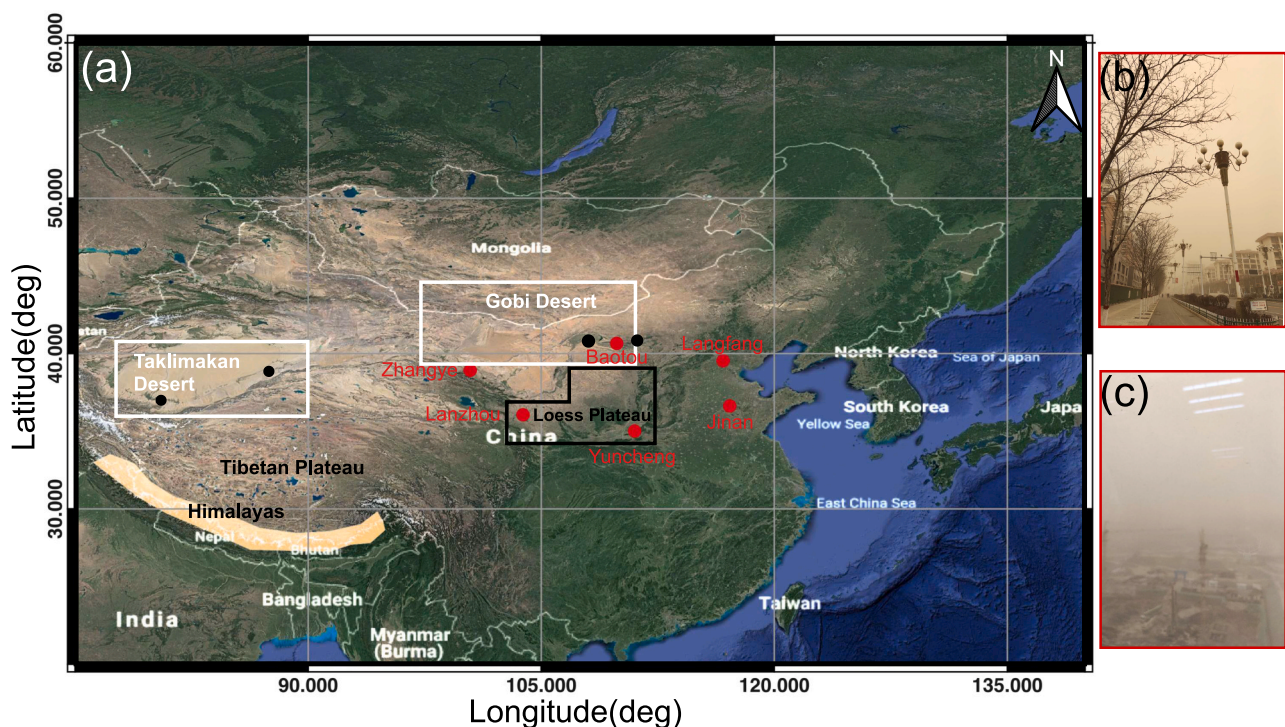


Fig. 2. Map of the study area. The Gobi Desert and the Taklamakan Desert are marked with white boxes. The black box shows the Loess Plateau. The location of the observation stations for the time series of the atmospheric pollutants, wind speed, and equivalent potential temperature (θ_e) are marked with red dots. Black dots mark the stations of the used radiosondes, namely (East to West) Hohoot, Linhe, Ruqiang, and Hotan. The images in (b) and (c) show scenes as seen during the dust event in Lanzhou. Map in (a) created with QGIS (QGIS Development Team, 2022).

was used to assess the observed vertical profiles of horizontal wind speed. It serves to identify Nocturnal Low-Level Jets (NLLJs) over the Taklamakan Desert in observational data.

2.2. Model data

For the spatial analyses of the meteorological developments of the event, we used data from three reanalysis data sets. The ERA5 reanalysis is the fifth generation of the European Centre for Medium-Range Weather Forecasts (ECMWF) reanalysis for 1950 to the present (Hersbach et al., 2020). It combines a modern weather model with observations from across the world into a globally complete and consistent atmospheric data set. ERA5 has a horizontal resolution of 0.25° . In this study, we used the mean sea-level pressure, as well as geopotential heights, temperature, humidity, and the zonal and meridional wind components at different levels over East Asia. We used the model output to also calculate θ_e at 850 hPa.

We use ERA5 data at different model levels to determine the spatial distribution of NLLJs over the Taklamakan Desert. NLLJs are identified with the automated detection algorithm, inspired by Fiedler et al. (2013) and Ge et al. (2016) as follows:

1. The vertical gradient of the virtual potential temperature must be larger than 0.001 km^{-1} in the first 100 m above the surface.
2. Wind speed maxima are identified between the lowest model level and 1000 m a.g.l.
3. The vertical wind shear must be stronger than -0.005 ms^{-1} in the 500 m deep layer above the wind speed maximum.

Based on ERA5 data, we also calculated back-trajectories for air masses arriving at the six selected urban stations at the point in time when the measured PM_{10} concentration reached its maximum. For this analysis, ERA5 data was used as input for the Hybrid Single-Particle Lagrangian Integrated Trajectory model (HYSPLIT; Stein et al., 2015; Rolph et al., 2017). For each station, trajectories were determined for three categories of heights between the surface and 3000 m a.g.l., with each comprised of three levels. The level categories were defined as low (10 m, 30 m and 50 m), medium (400 m, 600 m and 800 m) and high (1000 m, 2000 m and 3000 m). A grid of nine positions with a spacing of 0.25° around each station was used as starting points for the back-trajectories. In this way, an ensemble of 27 back-trajectories was obtained for each height category at all stations. From the time of maximum urban PM_{10} concentration, the back-trajectories were calculated with hourly increments until they either reach the boundaries of the study area (75°E – 145°E and 25°N – 60°N) or until seven days have been simulated. We computed the average across the 27 back-trajectories per height category for the stations. This approach allows us to show three ensemble-averaged back-trajectories per station with substantially reduced spatio-temporal variability to visualize the mean air-mass transport.

For quantitative estimates of dust emission, distribution, and transport, we use MERRA-2 reanalysis and CAMS forecasts. We chose two datasets to illustrate potential uncertainties in aerosol data sets for this case, which is expected based on previously documented data diversity for aerosols (e.g., Vogel et al., 2022; Zhao et al., 2022). MERRA-2 is the latest version of the global atmospheric reanalysis for the satellite era produced by the NASA Global Modeling and Assimilation Office (GMAO) using the Goddard Earth Observing System Model (GEOS; Molod et al., 2015). Dust aerosols in MERRA-2 is simulated for the five size bins: $0.1\text{--}1 \mu\text{m}$, $1\text{--}1.8 \mu\text{m}$, $1.8\text{--}3 \mu\text{m}$, $3\text{--}6 \mu\text{m}$, and $6\text{--}10 \mu\text{m}$. The MERRA-2 data has a horizontal resolution of $0.5^\circ \times 0.625^\circ$. Here the model output for the dust aerosol mixing ratio (GMAO, 2015a), dust emission and deposition (GMAO, 2015b), and dust aerosol optical depth (DOD; GMAO, 2015c) were used. Additionally, we used meteorological data from MERRA-2 and ERA5 to investigate the meteorological development of the event and to evaluate the re-analyses against station

observations for March 2021.

The atmospheric composition forecasts data from the Copernicus Atmosphere Monitoring Service (CAMS; Bozzo et al., 2020) of ECMWF has a horizontal resolution of 0.4° , and produces global forecasts for atmospheric composition twice per day. The forecasts include more than 50 chemical species (e.g., ozone, nitrogen dioxide, carbon dioxide) and seven different types of aerosols (desert dust, sea salt, organic matter, black carbon, sulfate, nitrate, and ammonium). Dust aerosols in CAMS forecasts are simulated for 3 size bins, namely $0.03\text{--}0.55 \mu\text{m}$, $0.55\text{--}0.9 \mu\text{m}$, and $0.9\text{--}20 \mu\text{m}$. CAMS, therefore, simulates larger dust sizes than MERRA-2. In our study, we used hourly data for aerosols from CAMS, namely the dust aerosol mixing ratio, dust emission, and deposition fluxes of desert-dust aerosols, as well as DOD. Using both MERRA-2 and CAMS allows us to quantify differences in dust simulations, e.g., shown for the dust emission fluxes.

2.3. Model validation

We used the station observation from NCDC to evaluate the representation of the meteorological conditions over the study region in MERRA-2 and ERA5 reanalysis. The data comparison is done for March 2021 to gain a statistic for the month when the dust event occurred. Here, 22 stations in the Gobi Desert and downwind, plus 10 stations in the Taklamakan Desert are selected for the data comparison. The inverse distance weighted average of the four nearest grid points for the temperature at 2 m a.g.l., and wind speed at 10 m a.g.l. from both MERRA-2 and ERA5 are calculated at each station. The comparison of the obtained means from the station observations with the reanalysis output suggested a good representation of the near-surface temperature development, indicated by the high positive Pearson's correlation coefficient (R) in the 2 m-temperature (Table 1) for all stations. R for local wind speed was lower than temperature, showing an average of 0.58 (MERRA-2) and 0.71 (ERA5) in the Gobi Desert, and 0.52 (MERRA-2) and 0.57 (ERA5) in the Taklamakan Desert. The Gobi Desert and downwind are relatively flat terrains and both MERRA-2 and ERA5 showed here higher R for wind speed than for the Taklamakan Desert. Higher R , particularly for ERA5, is seen to the East of 80°E in the Taklamakan Desert. Taken together, ERA5 is often better than MERRA-2 in representing the temporal evolution of temperature and winds. Hence, we often only show ERA5 in our presentation of the results for the atmospheric dynamics of the event, although qualitatively MERRA-2 and ERA5 show similar results.

3. Results

3.1. Overview and unusual characteristics of the dust event

We first analyze the synoptic-scale development of the dust event based on CAMS forecasts, MERRA-2 reanalysis, and ERA5 reanalysis (Fig. 3). At 14 BJT on 14 March, the upper-level jet stream was strongly meandering over East Asia (Fig. 3b). An embedded jet streak with wind speeds exceeding 60 ms^{-1} at 300 hPa was South of 50°N between 90°E and 110°E . At the poleward side of the jet streak a trough at 500 hPa extended from Northern Mongolia in the Southwest direction paired with a surface low to the East of the trough axis (Fig. 3c). The cold front from the center of the surface low to western Mongolia was visible as a horizontal gradient in θ_e at 850 hPa (Fig. 3d). Until 02 BJT on 15 March, the jet streak and the associated poleward low-pressure system moved south-eastward (Fig. 3f–g), accompanied by a southeastward propagation of the cold air mass (compare Fig. 3d and 3h). At the same time, the dust aerosols were transported southeastwards, showing a band of DOD from the Taklamakan Desert to the Gobi Desert in both CAMS forecasts and MERRA-2 reanalysis (Fig. 3e–f). The satellite image also indicated the dust aerosol layer stretching over most of the northern part of China a few hours later (Fig. 1a). At 20 BJT on 15 March, the jet streak shifted further south-eastward (Fig. 3j). The associated low-pressure system lay

Table 1
Validation of temperature at 2 m a.g.l., and wind speed at 10 m a.g.l. from MERRA-2 and ERA5 reanalysis compared to ground-based observations for 22 stations in the Gobi Desert and downwind (GD), and for 10 stations in the Taklamakan Desert (TD). Shown are the Pearson’s correlation coefficient (R) and root mean square error (RMSE) for the inverse-distance weighted averages of the four nearest grid points to each station location from MERRA-2 and ERA5 against the station observations.

	Station ID	Lat	Lon	Temperature				Wind speed			
				MERRA-2		ERA5		MERRA-2		ERA5	
				R	RMSE [°C]	R	RMSE [°C]	R	RMSE [ms ⁻¹]	R	RMSE [ms ⁻¹]
GD	545390	39.43	118.90	0.95	3.26	0.98	1.50	0.68	2.43	0.74	1.64
	528660	36.62	101.77	0.86	5.11	0.96	2.74	0.52	2.11	0.66	2.22
	548230	36.68	116.98	0.90	3.56	0.98	1.36	0.67	2.18	0.77	1.08
	526520	39.08	100.28	0.87	3.71	0.97	1.99	0.44	2.04	0.65	2.14
	533910	41.90	114.00	0.93	2.43	0.98	1.43	0.78	2.52	0.86	1.63
	524950	40.75	104.50	0.91	2.95	0.97	1.75	0.64	2.39	0.74	1.99
	522670	41.95	101.07	0.91	3.12	0.99	1.09	0.74	2.45	0.81	1.96
	548430	36.77	119.18	0.93	2.69	0.99	0.93	0.73	2.47	0.79	1.55
	536140	38.48	106.22	0.89	3.85	0.96	1.86	0.49	2.45	0.68	0.94
	535880	38.95	113.52	0.86	4.81	0.92	3.49	0.47	3.35	0.56	4.24
	539590	35.12	111.07	0.90	3.55	0.95	2.19	0.55	1.69	0.58	1.28
	539150	35.55	106.67	0.86	3.35	0.95	1.97	0.46	2.05	0.60	1.12
	538450	36.60	109.50	0.89	3.23	0.97	1.39	0.38	2.24	0.48	1.31
	532310	41.45	106.38	0.94	2.26	0.99	1.33	0.79	1.85	0.84	1.59
	536460	38.27	109.78	0.90	3.22	0.97	1.42	0.54	1.98	0.68	1.63
	537980	37.18	114.37	0.85	3.60	0.95	1.87	0.61	1.76	0.74	1.64
	535290	39.10	107.98	0.91	3.08	0.98	1.19	0.56	2.19	0.66	1.59
	533360	41.57	108.52	0.92	2.95	0.98	1.35	0.55	3.17	0.75	1.86
	544230	40.97	117.92	0.88	4.22	0.97	1.83	0.61	1.75	0.78	1.06
	526520	39.08	100.28	0.87	3.71	0.97	1.99	0.44	2.04	0.65	2.14
	525331	36.52	103.62	0.90	3.01	0.97	1.71	0.43	1.87	0.67	1.27
	545270	39.10	117.17	0.92	3.22	0.98	1.16	0.74	1.74	0.85	1.03
Mean				0.90	3.40	0.97	1.71	0.58	2.21	0.71	1.68
TD	518180	37.62	78.28	0.89	3.23	0.97	1.31	0.51	2.07	0.35	1.77
	516440	41.72	82.95	0.89	3.78	0.96	1.97	0.48	1.74	0.57	1.06
	517770	39.03	88.17	0.86	3.68	0.96	2.10	0.59	1.44	0.70	1.56
	517160	39.80	78.57	0.91	3.21	0.96	1.59	0.61	1.72	0.80	1.23
	516560	41.73	85.82	0.89	4.07	0.96	2.19	0.55	1.71	0.67	1.61
	517300	40.50	81.05	0.94	2.32	0.98	1.27	0.47	1.80	0.60	1.30
	518110	38.43	77.27	0.89	3.17	0.97	1.22	0.48	1.93	0.40	1.33
	517110	40.93	78.45	0.89	4.94	0.92	5.23	0.37	1.81	0.32	1.10
	517650	40.63	87.70	0.93	3.25	0.98	1.52	0.63	3.22	0.70	1.93
	518280	37.13	79.93	0.86	4.39	0.95	2.09	0.49	1.93	0.59	1.10
Mean				0.89	3.60	0.96	2.05	0.52	1.94	0.57	1.40

to the Northeast of the jet streak (Fig. 3k), and the cold air affected large areas North of 30°N (Fig. 3l). At 14 BJT on 16 March, the jet stream zonalised (Fig. 3n), and the further eastward movement of the surface low (Fig. 3o) resulted in a southeastward expansion of the cold air and a cold air intrusion into the Taklamakan Desert (Fig. 3p).

It is not surprising that a dust outbreak occurs due to a Mongolian cyclone in March 2021, but the characteristics of this case were unusual. The passage of Mongolian cyclones is a known driver of dust-emitting winds which may lead to dust storms in the Gobi Desert (Takemi and Seino, 2005). For quantifying how unusual this dust event was, we compare different variables observed during the dust event against climatological values for the 30-year period 1992–2021 (Fig. 4) based on ERA5 reanalysis and station observations. We further evaluate the spatio-temporal distributions of PM₁₀ concentrations and atmospheric visibility to illustrate the impacts of the dust outbreak in Chinese cities (Fig. 5).

The time series for the near-surface temperature anomaly indicated an increase in near-surface air temperature in the Gobi Desert preceding the onset of the dust event (Fig. 4a). This temperature increase was not limited to the Gobi Desert but was also seen further North, South, and Northeast of the desert as indicated by ERA5 reanalysis (Fig. 4b). High temperatures favored the melting of snow and evaporation from the soil. It leads to exposing and drying of bare soil, as a prerequisite for later dust emissions. A sudden decrease in near-surface temperature occurred in the Gobi Desert from 14 to 15 March along with cold air advection by the Mongolian cyclone (Fig. 4a). The occurrence of the cyclone is also seen in the anomaly of the mean sea level pressure during the dust event, with regionally 15 hPa lower mean sea level pressure than the 1st

percentile of the March climatology for 1992–2021 (Fig. 4c). The cyclone was associated with maximum 10 m wind speeds over Mongolia and northeastern China between the 13 and 18 March 2021 which exceeded the 99th percentile of the wind statistics for 1992 to 2021 by far. Particularly strong winds occurred in the middle of Mongolia. Here, the wind speed exceeded the 99th percentile by around 6 ms⁻¹ (Fig. 4d). The maximum near-surface winds in the Gobi Desert were sufficiently strong for dust-aerosol emissions (Fig. 1b), e.g., they were much stronger than the previously estimated thresholds for dust emission onset of 9.8±2.2 ms⁻¹ to 13.8±2.0 ms⁻¹ for this region (Kurosaki and Mikami, 2007).

As we will see later, the dust was elevated over the source regions and transported southeastwards, leading to low visibility in metropolitan areas across China (Fig. 4e–f). Specifically, 45 out of 218 Chinese stations recorded visibility minima lower than 1000 m to the North of 30°N (Fig. 4e). For 23 stations, the visibility was even below 500 m. Only in March 2002, more stations reported visibility below 1000 m than in March 2021. Most strikingly, 19 stations in northern China, marked by a black dashed box in Fig. 4f, recorded the lowest visibility for March in the past 30 years assessed here. These results underline the exceptionally low visibility and the large spatial extent of the impacts of the dust outbreak in March 2021.

The spatio-temporal variations seen in station observations suggested a southeastward propagation of the dust-laden air for 15–16 March 2021 (Fig. 5a–d), consistent with the movement of the cold air and DOD in forecasts and reanalysis (Fig. 3). Furthermore, MERRA-2 reanalysis suggested that the lifted dust aerosols were transported further eastwards and passed the Pacific Ocean in the next week (not

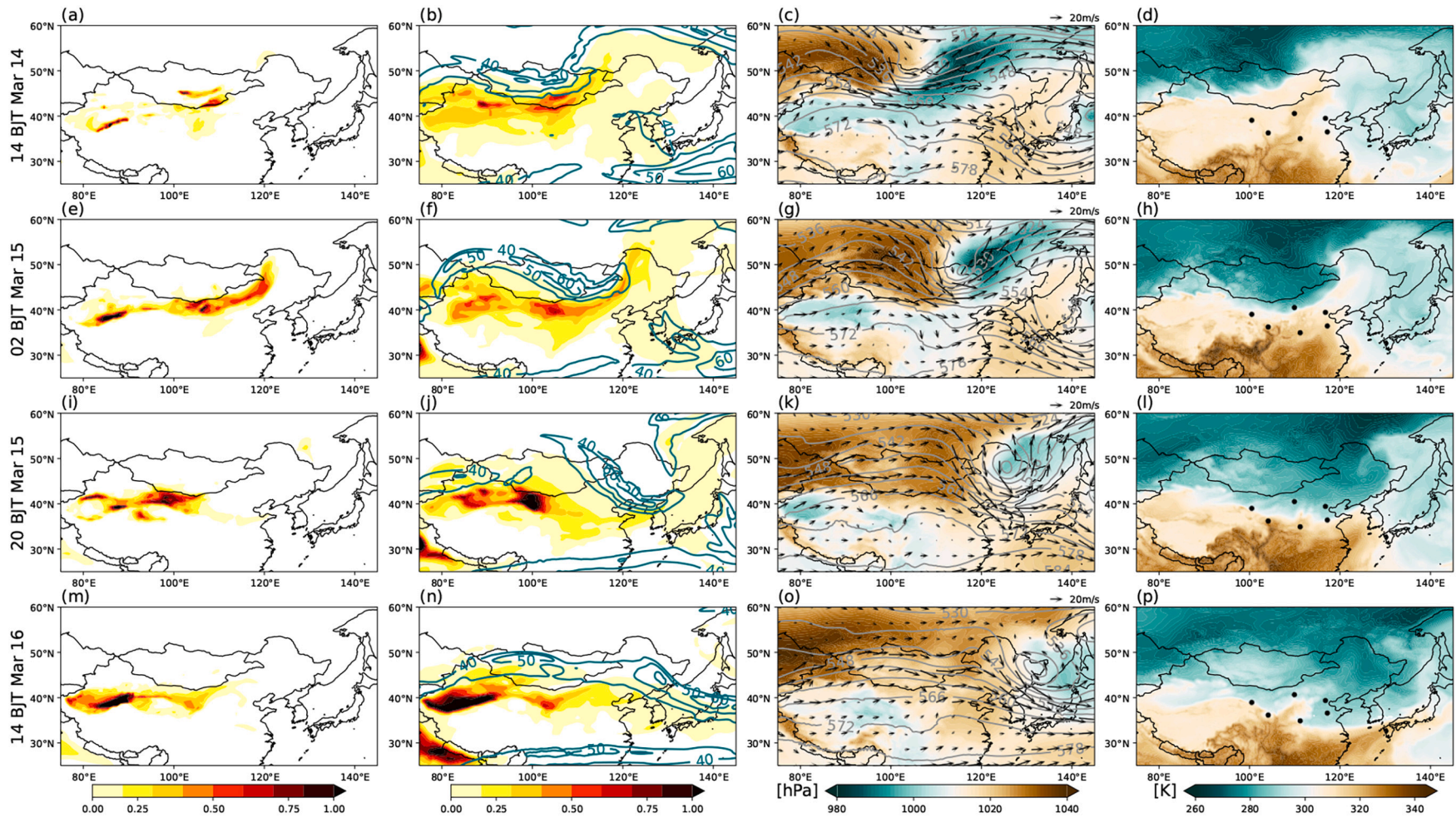


Fig. 3. Meteorological dynamics of the dust event. Shown are (1st column) DOD from CAMS forecast (shading), (2nd column) DOD from MERRA-2 reanalysis (shading), and 300 hPa horizontal winds for illustrating the jet stream (contours, units: ms^{-1}), (3rd column) 500 hPa winds vectors (arrows), 500 hPa geopotential height (contours, units: dam), and mean sea-level pressure (shading), and (4th column) 850 hPa equivalent potential temperature (shading) on (a–d) 14 March 2021 at 14 BJT, (e–h) 15 March 2021 at 02 BJT, (i–l) 15 March 2021 at 20 BJT, and (m–p) 16 March 2021 at 14 BJT. Black dots mark the locations of the six cities. Meteorological data is from ERA5.

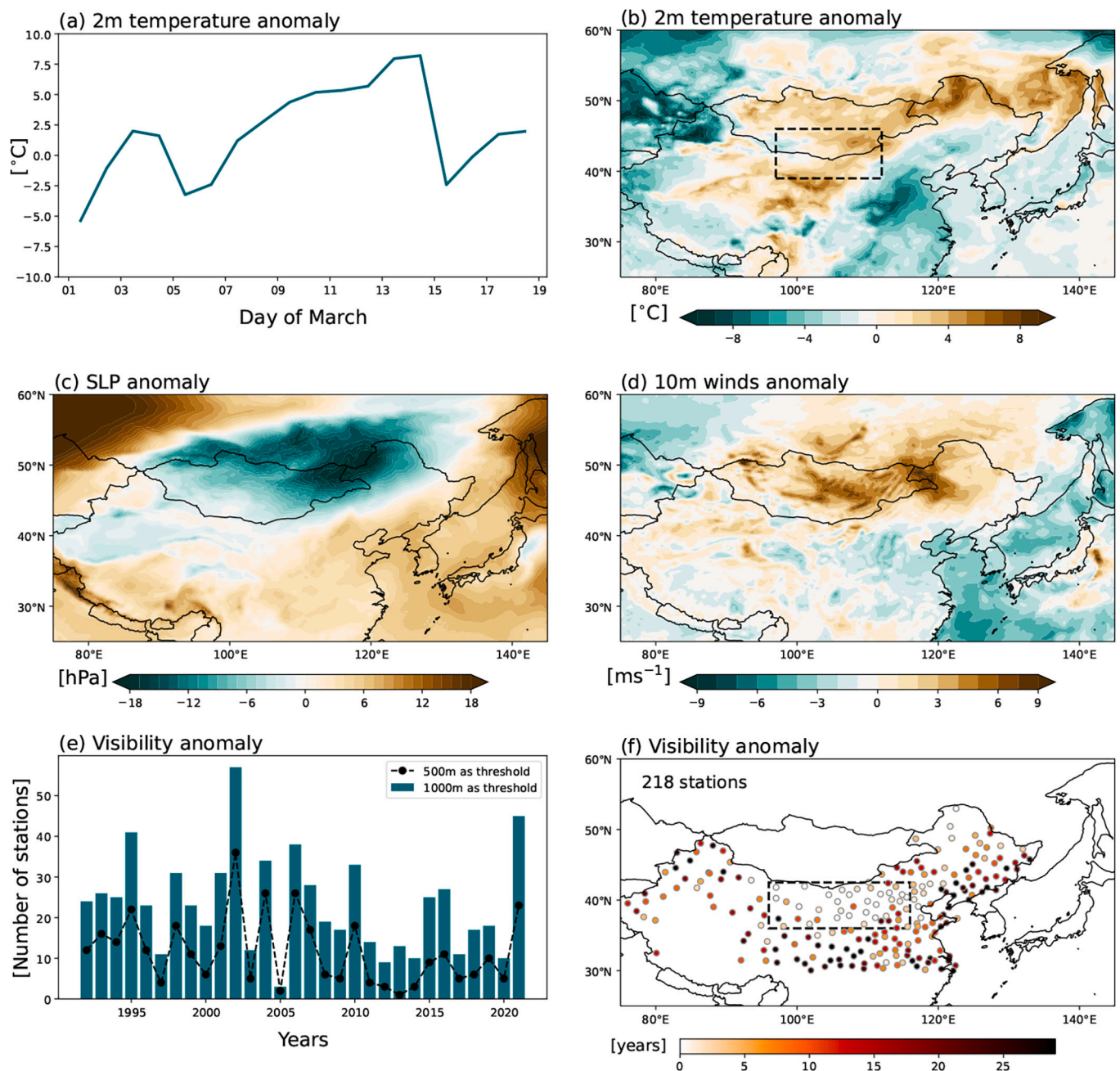


Fig. 4. The unusual characteristics of the dust event. Shown are (a) time series of 2 m-temperature anomaly (blue solid line) in the Gobi Desert (97°E–112°E, 39°N–46°N) marked by black dashed box in (b) for 1–18 March 2021 with respect to the March 1992–2021 climatology, (b) the difference between the 6–14 March 2021 maxima and the 99th percentile for the March climatology of 1992–2021 for the 2 m-temperature, (c) like (b) but for the minimum mean sea level pressure against the 1st percentile of the March climatology 1992–2021, (d) like (c) but for the maximum 10 m-wind speed against the 99th percentile of the March climatology 1992–2021, (e) the number of stations with a recorded minimum visibility under 1000 m (histogram) and 500 m (line) in March for each year, and (f) the number of years when the recorded minimum visibility in the March statistics for 1992–2020 was smaller than for this dust event (13–18 March 2021). Note that other phenomena that reduce visibility like fog have been eliminated prior to this analysis (see method section). Figures a,b,c,d based on ERA5 reanalysis, and e,f on station observations in China.

shown). However, high PM₁₀ concentrations and low atmospheric visibility were limited to western China on 17 and 18 March (Fig. 5e–h), when the Mongolian cyclone and its embedded cold front already had passed the Gobi Desert (Fig. 3). These results indicate spatial differences during the dust event, which will be assessed in detail in the next two sections.

3.2. Dust emission mechanisms

To better understand the atmospheric dynamics in different dust source regions leading to the dust outbreak, we first assess the temporal development of the dust-aerosol emission and deposition fluxes for particle sizes of 0.1–10 μm (MERRA-2 reanalysis), and 0.03–20 μm (CAM5 forecasts) in the Gobi Desert, the Taklamakan Desert, and the Loess Plateau. To that end, we here compute spatial averages of dust-aerosol fluxes for all potential dust sources in the three regions

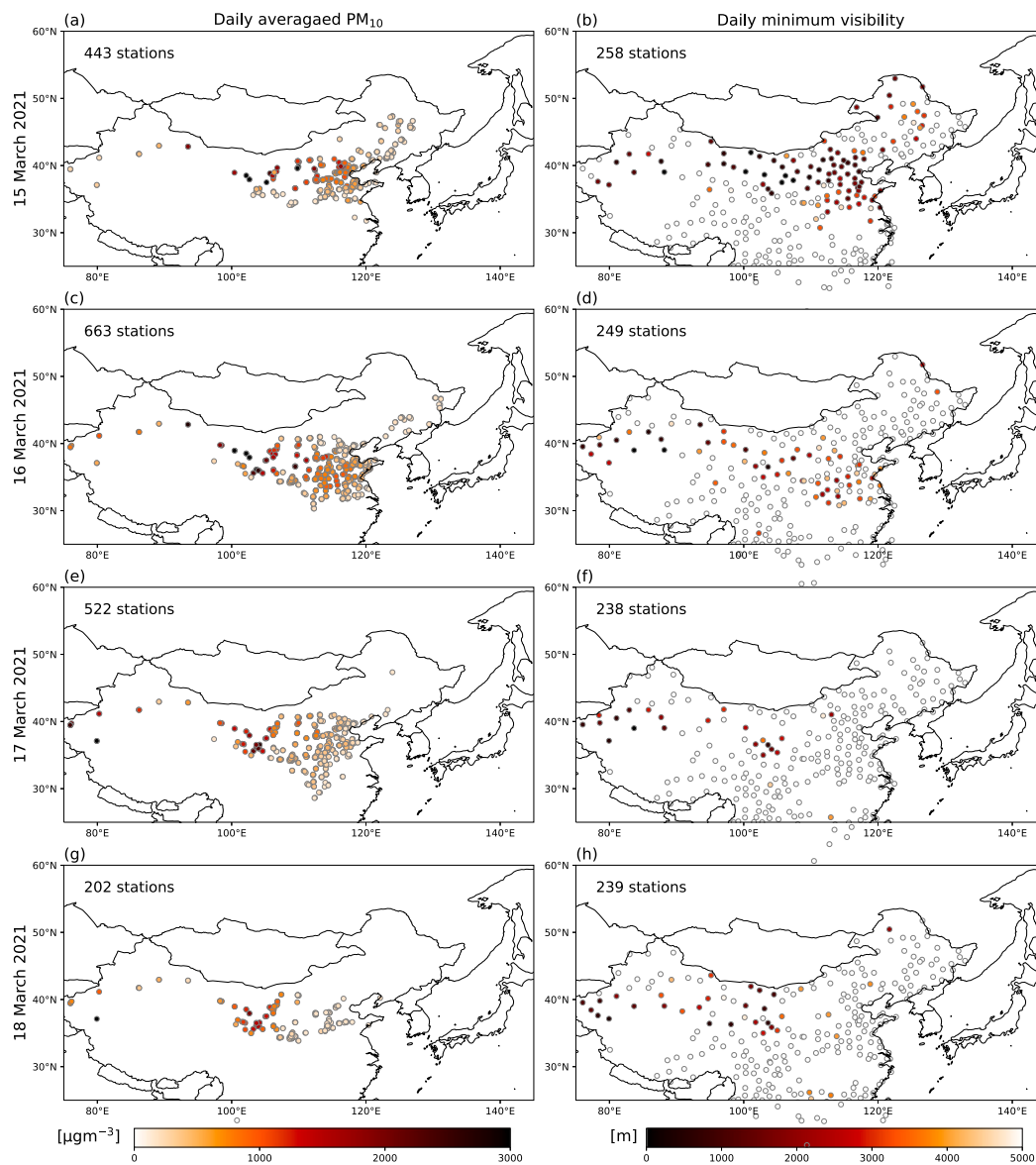


Fig. 5. Dust recordings at stations in China. Shown are (left column) the daily average PM_{10} concentrations, and (right column) daily minimum visibility on (a–b) 15 March, (c–d) 16 March, (e–f) 17 March, and (g–h) 18 March 2021. Data based on in situ observations in China. Only stations with record PM_{10} concentrations higher than $150 \mu\text{g m}^{-3}$ are shown.

(Fig. 6) and examine the vertical profiles of horizontal winds at four radiosonde stations in the Gobi Desert and the Taklamakan Desert (Fig. 7). We then present longitude-height cross-sections for the dust mixing ratio, horizontal winds, and θ_e along transects in the Gobi Desert, namely 100°E , 50°N to 112°E , 35°N marked by the blue line in Fig. 8a, and in the Taklamakan Desert, namely from 80°E , 38°N to 95°E , 42°N shown as the blue line in Fig. 9a. The transect in the Gobi Desert approximately follows the path of the cold front in this event, while the transect in the Taklamakan Desert follows the typical dust-aerosol transport path for spring, documented by Yuan et al. (2019).

In the mid-March 2021 case, the passage of the Mongolian cyclone facilitated dust emissions in both the Gobi Desert and the Taklamakan Desert. We analyzed dust emission and deposition from both MERRA-2 reanalysis and CAMS forecasts. The dust emission and deposition fluxes from CAMS were systematically higher than that from MERRA-2. A possible reason is that CAMS simulates a larger range in particle sizes compared to MERRA-2. Although the fluxes from the datasets differed in magnitude, the datasets agree on the time of increases in the dust emission flux in the Gobi Desert and the Taklamakan Desert (Fig. 6a–b)

during the occurrence of the extra-tropical cyclone (compare Fig. 6a–b and 3). More specifically, dust emission in the Gobi Desert started to increase at 08 BJT on 14 March (in both MERRA-2 and CAMS), and reached its maximum at 14 BJT (CAMS forecasts) and 17 BJT (MERRA-2 reanalysis) on 14 March (Fig. 6a). In the Taklamakan Desert, maximum dust emissions were observed later at 04 BJT (MERRA-2) and 05 BJT (CAMS) on 16 March, which was the time when the cold air arrived in this desert (Fig. 3l, p). Averaged over the Loess Plateau, the deposition flux exceeded the emission flux, indicative of this region acting as a net sink for dust aerosols (Fig. 6c, f). Also during past severe dust outbreaks recorded in the Loess Plateau, dust particles were transported from the Taklamakan and the Gobi Desert to the Plateau rather than being locally emitted by strong winds (Huang et al., 2008). Details on the dust emission mechanisms in the Gobi and Taklamakan Desert are discussed next.

3.2.1. Gobi Desert

Dust-aerosol emissions in the Gobi Desert coincided with the passage of the Mongolian cyclone. At 17 BJT on 14 March, the Northwest to

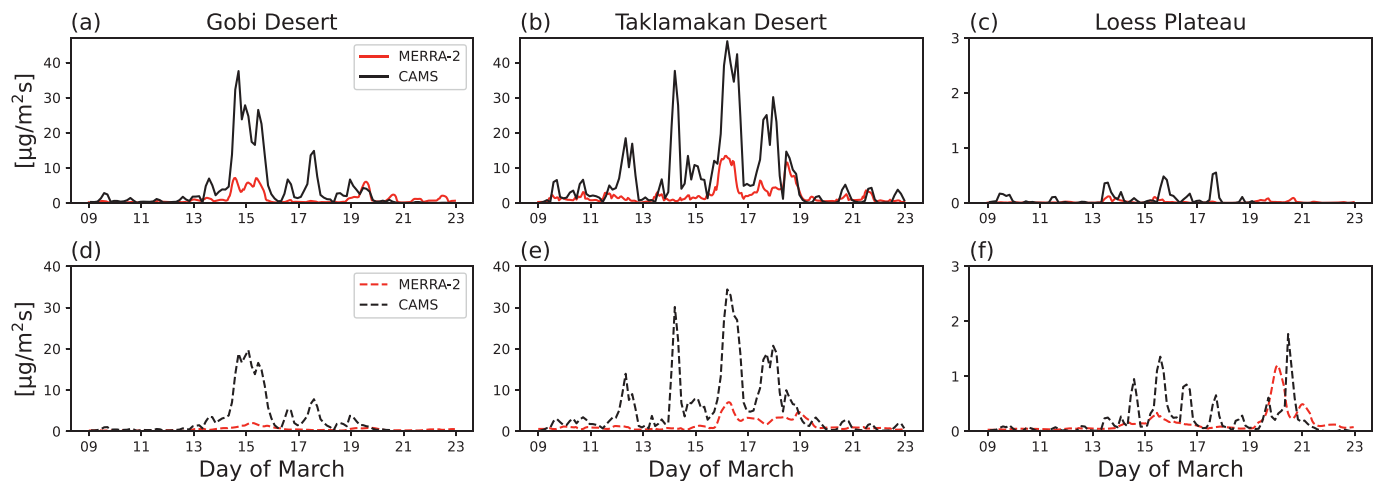


Fig. 6. Dust emission and deposition in East Asia. Shown are (a–c) time series of spatially averaged dust-aerosol emission fluxes for the Gobi desert (97°E–112°E, 39°N–46°N), the Taklamakan Desert (77°E–90°E, 36°N–41°N), and the Loess Plateau (101°E–108°E, 34°N–37°N plus 108°E–114°E, 34°N–39°N), (d–f) like (a–b) but for dust deposition fluxes.

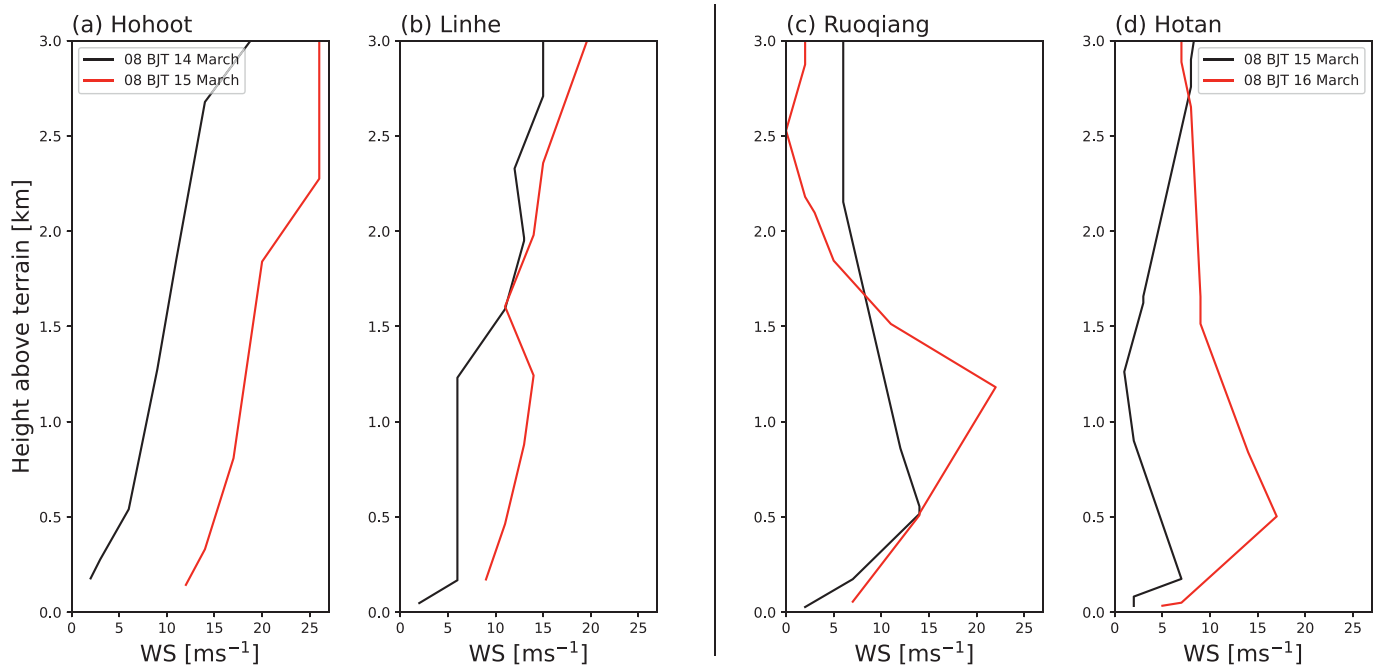


Fig. 7. Wind profiles in the Gobi and Taklamakan Desert during the dust event. Shown are the vertical distribution of horizontal wind speed from radiosondes launched at (a) Hohoot and (b) Linhe for 08 BJT on 14 March (black lines) and 08 BJT on 15 March (red lines) in the Gobi Desert, and at (c) Ruoqiang and (d) Hotan for 08 BJT on 15 March (black lines) and 08 BJT on 16 March (red lines) in the Taklamakan Desert.

Southeast cross-section for the Gobi Desert showed a strong horizontal gradient in θ_e around 103°E indicating the position of the cold front of the cyclone (Fig. 8c). At the same time, there were relatively strong upward winds in a zone from 104°E to 107°E. These favored the deep upward mixing of the freshly deflated dust particles over the Gobi Desert, supported by MERRA-2 reanalysis (Fig. 8e) and CAMS forecasts (not shown). At 08 BJT on 15 March, when the cyclone and the associated cold front moved eastwards (Fig. 3b–l), the dust emission reached regions further South (Fig. 8b, d, f). Radiosondes measured winds of 10–20 ms^{-1} in the lowest 2 km a.g.l. during the morning of 15 March over the Gobi Desert (Fig. 7a–b), which were sufficiently strong (larger than the dust emission thresholds: $9.8 \pm 2.2 \text{ ms}^{-1}$ to $13.8 \pm 2.0 \text{ ms}^{-1}$; Kurosaki and Mikami, 2007) to emit and transport dust aerosols. Dust aerosols were exported from the Gobi Desert, indicated by the larger spatially averaged dust-aerosol emission compared to the dry deposition

over the Gobi Desert (Fig. 6a, d). Note that the Taklamakan Desert had little dust source activation at that time (Fig. 6b).

3.2.2. Taklamakan Desert

In the Taklamakan Desert, dust source activation is typically more frequent than in the Gobi Desert (Tao et al., 2022). This is also seen in March 2021, when daily emission events between 9 and 23 March occurred in the Taklamakan whereas dust sources in the Gobi were activated on fewer days (Fig. 6a–b). We assess here the spatial variations in dust emission fluxes from MERRA reanalysis and height-longitude transects for θ_e , dust mixing ratio, and winds along with spatial maps of dust emission fluxes on 10 and 13 March at 14 BJT (prior to the dust outbreak from the Gobi) and on 16, 17, and 18 March at 05 BJT (after the passage of the Mongolian cyclone) to better understand the dust emission mechanisms in the Taklamakan Desert (Fig. 9).

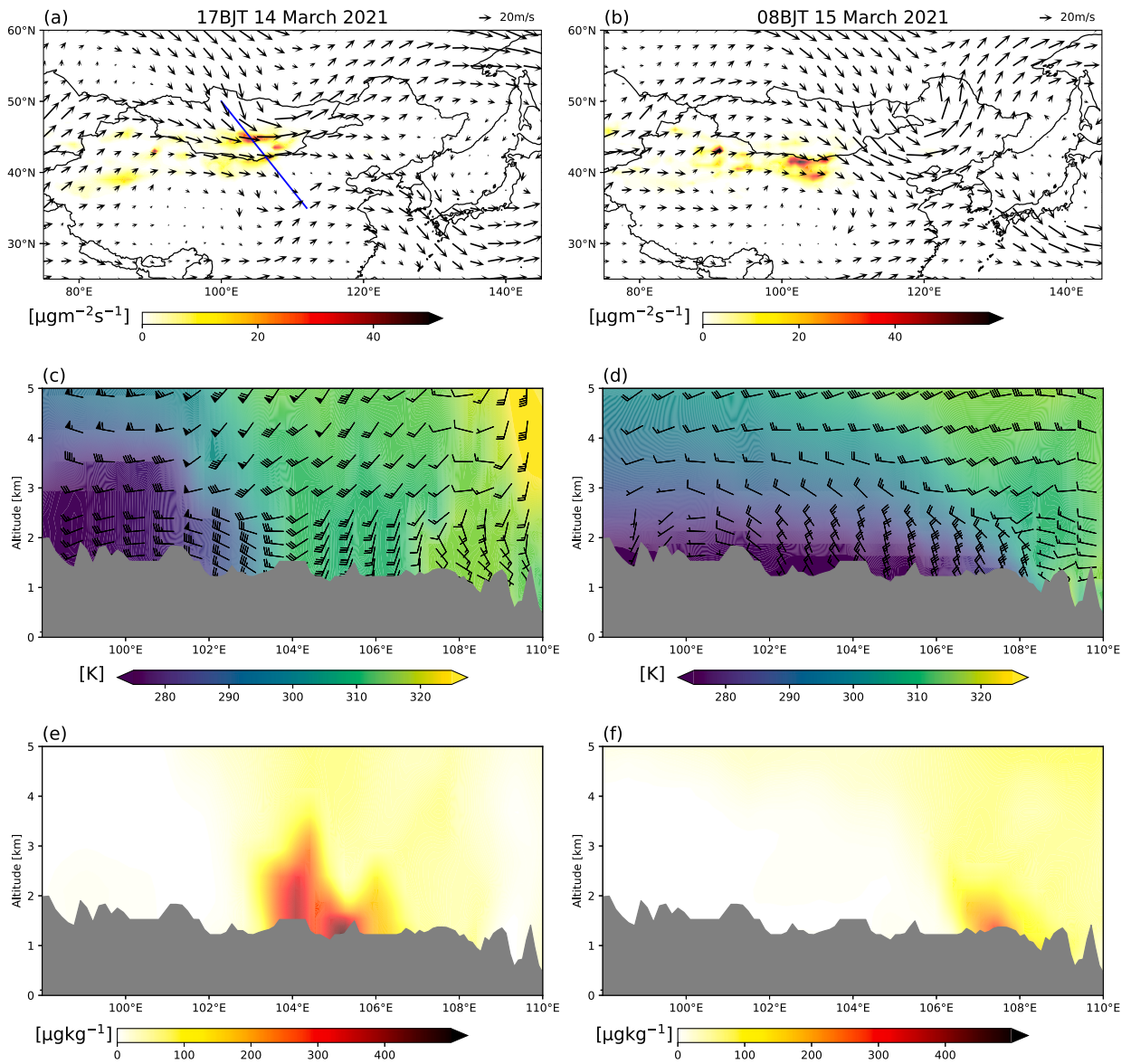


Fig. 8. Dust aerosols from the Gobi Desert in this event. Shown are dust emission fluxes from MERRA-2 (shading) and 500 hPa winds from ERA5 (arrows) on (a) 14 March at 17 BJT and (b) 15 March at 08 BJT, the vertical cross-sections for θ_e and winds from ERA5 along the transect marked with a blue line in (a) on (c) 14 March at 17 BJT, and (d) 15 March at 08 BJT. (e–f) like (c–d) but for the dust mixing ratio from MERRA-2.

We found Nocturnal Low-level Jets (NLLJs) associated with the cold air intrusion in the mid-March 2021 dust case in the Taklamakan Desert. NLLJ can form during near-surface stable stratification (Blackadar, 1957), which may arise from nocturnal cooling and, like in our case, also the advection of cold dense air at near-surface levels. In the early morning of 16 March, the Taklamakan Desert was under the influence of the near-surface cold air that was subsequently advected from the East (Fig. 9h). At that time strong dust emissions occurred in the Taklamakan along with strong near-surface easterlies between the surface up to 2 km height (Fig. 9g–h). Although weaker in magnitude, dust-source activation was also seen in the morning hours of the following two days on 17–18 March 2021 (Fig. 9j, m). The cold air and the persistent near-surface easterlies on these days led to the formation of easterly nocturnal low-level jets (NLLJs) seen in the re-analysis and measured by radiosondes in the desert (Fig. 7c–d).

The advection of cold air in the wake of the cold front of the Mongolian cyclone led to a near-surface temperature reduction and formation of near-surface inversions over the Taklamakan Desert, as indicated by increasing θ_e with height (Fig. 9h, k, n). Surface inversions are a

prerequisite for NLLJ developments (Fiedler et al., 2013; Alizadeh-Chooabari et al., 2014; Ge et al., 2016). The reduced frictional effects during the stable stratification allow the air in some distance to the surface to accelerate in the course of the night, which leads to a NLLJ (e.g., Van de Wiel et al., 2010).

The NLLJ breakdowns contributed to building a dust layer over the Taklamakan. The momentum transfer during the breakdown of NLLJs is a known process for dust emission in several deserts. In order to illustrate the effects of the NLLJ breakdown on the near-surface wind speed, we show the wind speed at 10 m a.g.l. at 11 BJT (about 09 LT) for 15–18 March (Fig. 10), which is the time for NLLJs breakdown from dust source regions in North Africa and the Taklamakan Desert (e.g., Fiedler et al., 2013; Heinold et al., 2013; Ge et al., 2016). We further quantify the wind speed difference in the core of the NLLJs on these days against the March climatology for 1992–2021 to assess the strength of the NLLJs at night (05 BJT, about 03 LT) during the cold air intrusion compared to mean conditions (Fig. 10). On 16 March at 05 BJT, when the cold air was in the Taklamakan Desert (Fig. 3l, p), strong NLLJs and near-surface winds occurred, particularly in the eastern part of the desert, where

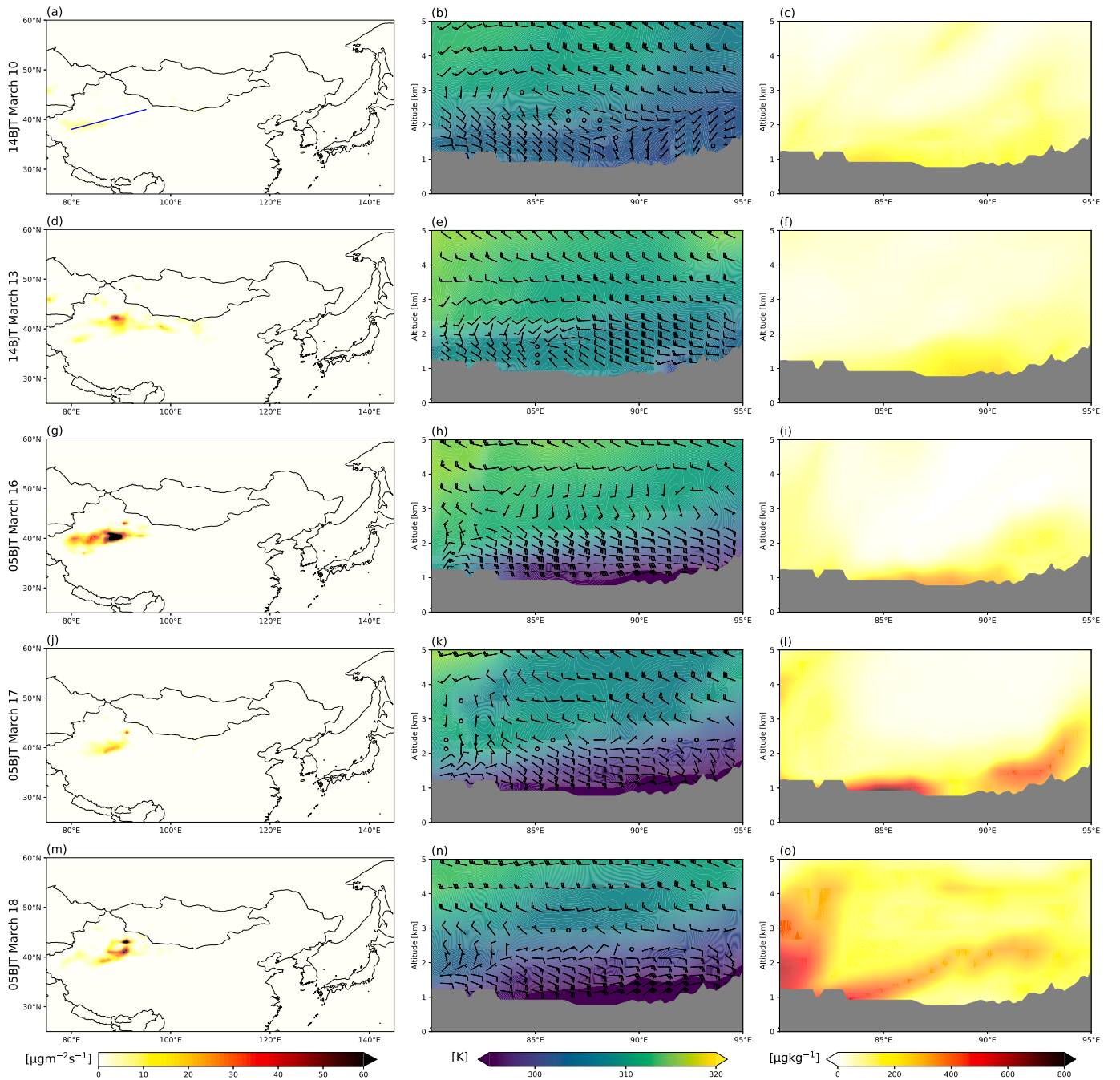


Fig. 9. Dust aerosols from the Taklamakan Desert. Shown are (left column) dust emission fluxes from MERRA-2, (middle column) the vertical cross-sections for θ_e (shading) and winds (arrows) from ERA5 along the transect marked with a blue line in (a), and (right column) vertical profiles of the dust mixing ratio from MERRA-2 for particle sizes of 0.1–10 μm along the transect on (a–c) 10 March at 14 BJT, (d–f) 13 March at 14 BJT, (g–i) 16 March at 05 BJT, (j–l) 17 March at 05 BJT, and (m–o) 18 March at 05 BJT.

the NLLJs core wind speed exceeded the 30-year climatology by around 6 ms^{-1} (compare Fig. 10a–c and e–g). The winds were sufficiently strong and exceeded the dust emission thresholds in the Taklamakan Desert of $4.4 \pm 0.6 \text{ ms}^{-1}$ to $6.7 \pm 1.5 \text{ ms}^{-1}$ (Kurosaki and Mikami, 2007). Accordingly, high dust emission occurred in the Taklamakan Desert, indicated by both MERRA-2 and CAMS (Fig. 6b). At 11 BJT, the wind speed at 10 m a.g.l. was still strong, leading to dust emissions (Fig. 6b). In the next two days (17–18 March) at 05 BJT, NLLJs with core wind speeds of about 12 ms^{-1} occurred, which were still higher than the 30-year climatology (Fig. 10i, j, m, n). Although the NLLJs and 10 m wind

speeds were weaker compared to 16 March, the mid-morning breakdown of NLLJs due to turbulent mixing led to near-surface peak winds in the Taklamakan Desert that were sufficiently strong for further dust emissions (Fig. 10l, p). Accordingly, the dust aerosol emissions reached values of $6.3 \mu\text{gm}^{-2}\text{s}^{-1}$ (MERRA-2) at 11 BJT on 17th, and $11.5 \mu\text{gm}^{-2}\text{s}^{-1}$ (MERRA-2) and $14.6 \mu\text{gm}^{-2}\text{s}^{-1}$ (CAMS) at 11 BJT on 18th March 2021 over the Taklamakan Desert (Fig. 6b). The strong near-surface easterlies led to an initial westward transport near the surface and deep upwards mixing of dust aerosols, particularly over the west of the Taklamakan Desert for 16–18 March (Fig. 9h, i, k, l, n, o). The dust aerosols were here

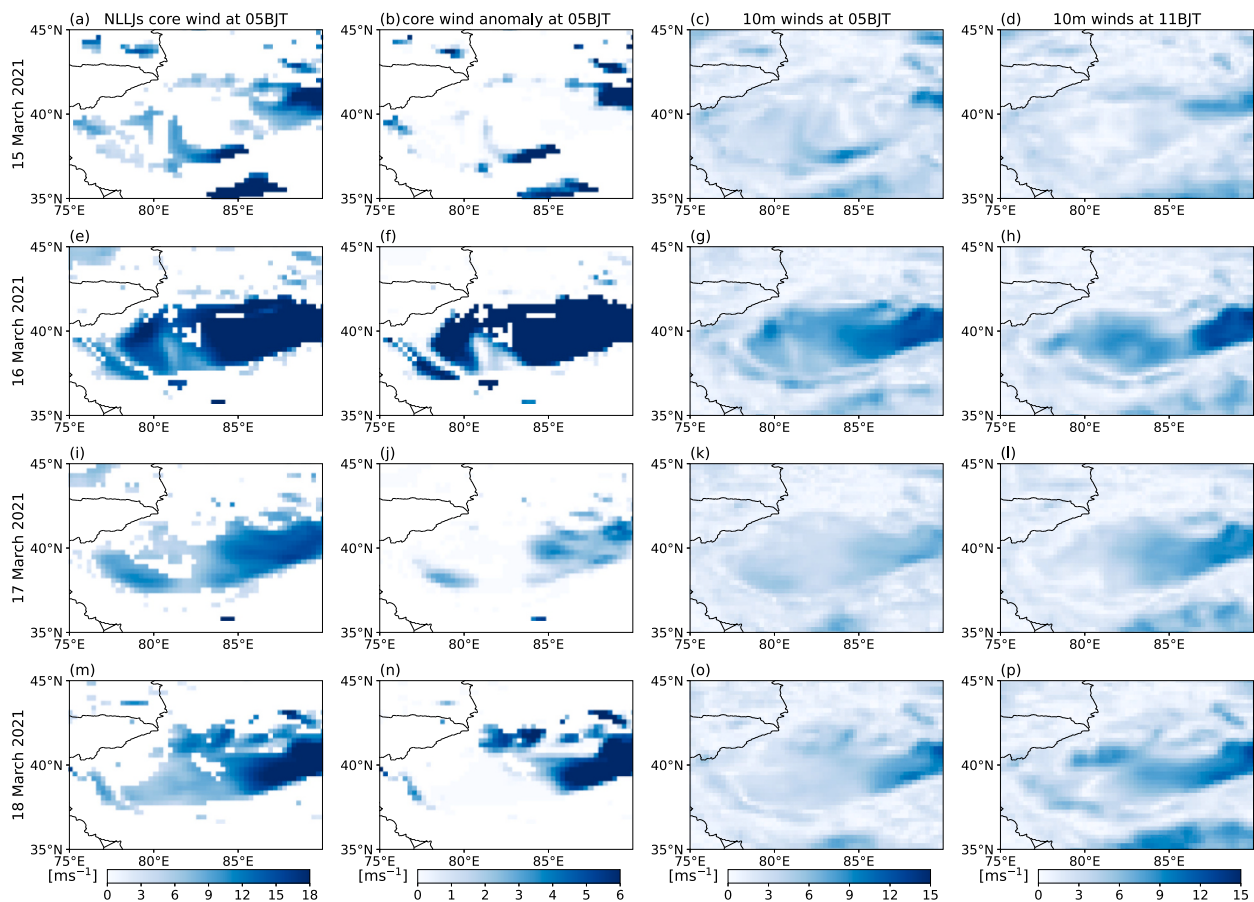


Fig. 10. Nocturnal Low-Level Jets (NLLJs) in the Taklamakan Desert during the event. Shown are (1st column) NLLJs core winds at 05 BJT, (2nd column) NLLJs core wind anomalies at 05 BJT with respect to the March climatology for 1992–2021, (3rd column) wind speed at 10 m a.g.l. at 05 BJT, and (4th column) wind speed at 10 m a.g.l. at 11 BJT on (a–d) 15 March, (e–h) 16 March, (i–l) 17 March, and (m–p) 18 March 2021. NLLJs are identified with an automated detection algorithm in ERA5 reanalysis data.

lifted to sufficiently high levels to later overcome the topographic barrier at the Eastern margin of the desert. The additional emissions and deep turbulent mixing build a dust layer over the Taklamakan extending to a height of at least 5 km (Fig. 9l, o).

3.3. Influence of dust on urban air quality

Dust aerosols are known to have serious impacts on air quality (De Longueville et al., 2010; Rashki et al., 2012; Li et al., 2018; Wang et al., 2020). To better understand the spatial differences in the impact of the dust event on air quality in Chinese cities in the 2021 dust outbreak, six cities in the northern regions of China are selected (details in Section 2.1). We assess the temporal development of the cold front, paired with AQI, PM_{2.5}, PM₁₀ and the ratio between PM_{2.5} and PM₁₀ (Fig. 11). Back-trajectories are calculated as indicators for potential sources of the dust aerosols (Fig. 12).

In most of the six cities, the passage of the cold front was clearly marked by an increase in near-surface wind speeds that was accompanied by a distinct increase in the concentrations of PM₁₀ (Fig. 11). In our case, the dust aerosols were transported southeastwards ahead of the cold air in the southwestern sector of the Mongolian cyclone, which was also characterized as a region between two neighboring convergence lines of 850 hPa anomalous winds (Qian et al., 2022). Low-level convergence creates lifting of the air mass, reflected in our results as deep turbulent mixing as seen in the vertical velocities and the deep mixing of dust aerosols over several kilometers depth (Fig. 8). The first cities to be affected by the dust aerosols were Zhangye (Fig. 11a–b), Baotou (Fig. 11e–f), and Langfang (Fig. 11i–j) in the North, while the

three southern cities experienced an increase in PM₁₀ concentration later (Fig. 11). Consequently, the highest PM₁₀ concentrations among the six cities ranged from around 2000 to 5000 $\mu\text{g m}^{-3}$, which was in the same order of magnitude as previous dust storms in East Asia and the Middle East (Guan et al., 2019; Hamzeh et al., 2021). After the cold front had passed, near-surface winds weakened while the accumulated dust aerosols in the atmosphere persisted, also known from other regions, e.g., the Arabian Sea (Rashki et al., 2019). As a result, high PM₁₀ concentrations in the six cities were observed even several hours after the passage of the cold front (Fig. 11). Amongst the six cities, Zhangye and Langfang recorded their highest hourly PM₁₀ concentrations during this event since the beginning of the record in 2015 (not shown). As a consequence of the PM₁₀ increases, the AQI simultaneously increased and reached the maximum value of 500 in all cities (right column in Fig. 11). The critical level of 300 for health risks was therefore exceeded by far, which led to warnings for risk groups (Hu et al., 2015).

The urban air quality was affected by dust aerosols from several source regions in both the Taklamakan and Gobi Desert during this dust event. The influence of high PM₁₀ concentrations in the two westernmost cities, Zhangye and Lanzhou, were longer than in the other four cities (right column in Fig. 11). The back-trajectories arriving in these two western cities crossed both the Taklamakan and the Gobi Desert (Fig. 12a–b), suggesting possible contributions of dust aerosols from both deserts. The back-trajectories further indicated that the air masses passed the Taklamakan Desert on 10 and 13 March when PM₁₀ concentrations maxima were first recorded in the two western cities, Zhangye and Lanzhou (Fig. 11b, d and 12a–b). During mid-day on 10 and 13 March, there were layers with dust aerosols and westerlies

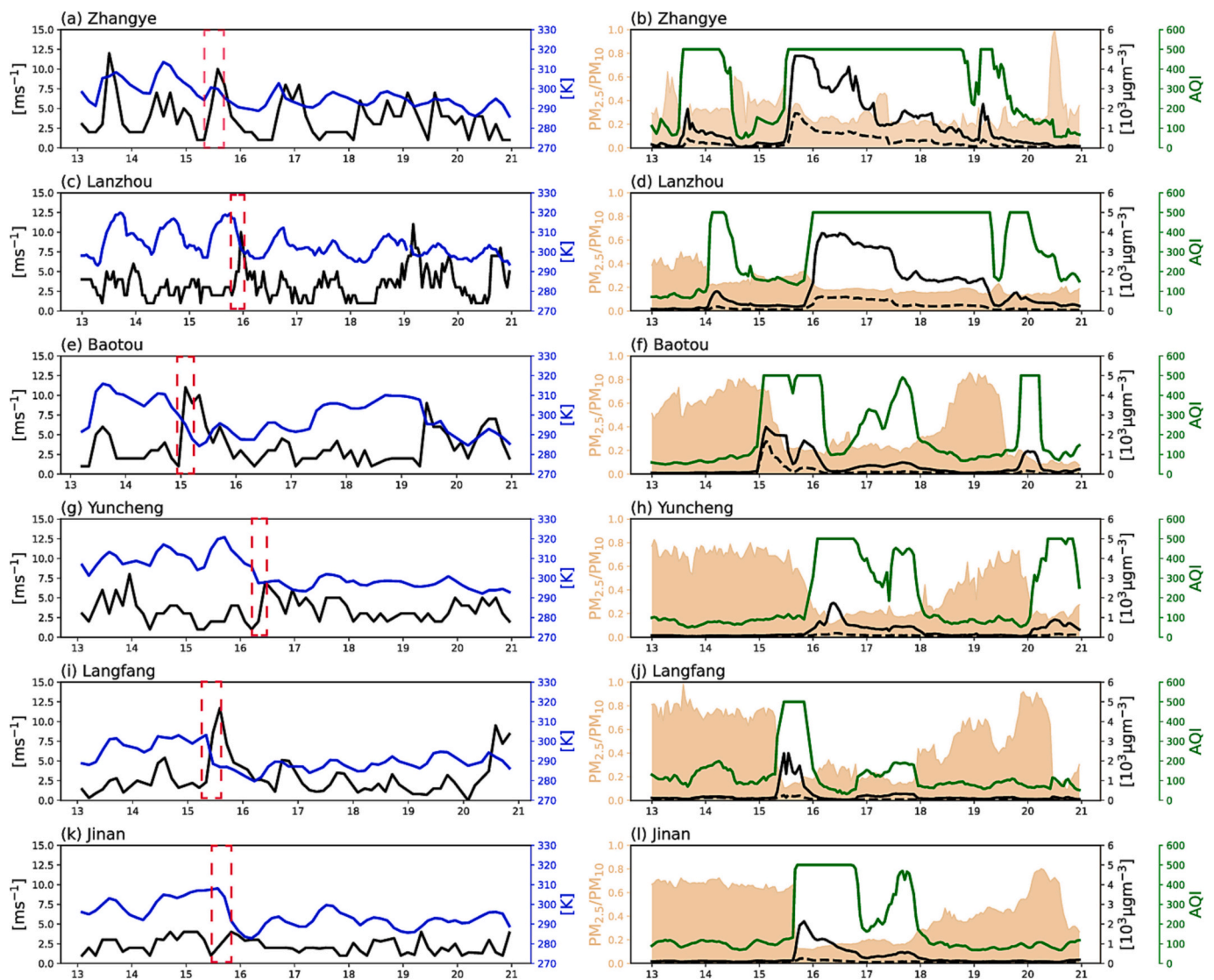


Fig. 11. Time series of meteorological and air quality measurements from city stations. Shown are (left column) 10 m-wind speed (black line) and equivalent potential 2 m-temperature (blue line), and (right column) $PM_{2.5}$ (black dashed line), PM_{10} (black solid line), Air Quality Index (AQI, green solid line) and the ratio between $PM_{2.5}$ and PM_{10} (shading) for (a–b) Zhangye, (c–d) Lanzhou, (e–f) Baotou, (g–h) Yuncheng, (i–j) Langfang, and (k–l) Jinan. Red lines in the left panels mark the sharp increase in wind speed associated with the passage of the cold front (compare to 4th column in Fig. 3).

between the surface and at least a height of 5 km a.g.l. in the Eastern part of the Taklamakan Desert paired with ongoing activation of dust sources (Fig. 9a–f). These conditions allowed the eastward transport of dust-laden air over the topographic barrier at the Eastern margin of the Taklamakan (Chen et al., 2017). Indeed, we see that the ratio between $PM_{2.5}$ and PM_{10} hardly decreases in the two western cities, Zhangye and Lanzhou, pointing to a larger amount of fine particles in the West than at stations further East. This is consistent with the typically smaller dust particles from the Taklamakan Desert (1.0–2.5 μm ; Zhao et al., 2015) affecting the western stations, compared to transported dust from the Gobi Deserts which is relatively larger in particle sizes (larger than 2.5 μm) and also affects the eastern stations during mid-March 2021 event. The back-trajectories further indicate a partial mixture of air in the central cities, Baotou and Yuncheng. The back-trajectories arriving in medium and low levels here indicated the transport of air masses from the northwest, thus passing the Gobi Desert (Fig. 12c–d). However, the back-trajectories arrived at higher levels between 1 and 3 km a.g.l. pointed to the transport of air masses from the west and in the case of Baotou also passed the Taklamakan Desert. The back-trajectories for the easternmost cities, Langfang and Jinan (Fig. 12e–f) were similar to each

other. For all three heights, the air masses here followed trajectories coming from the Northwest and thus passing solely the Gobi Desert, which suggests that dust from the Taklamakan Desert did not affect the eastern cities.

After the dust storm onset over the Gobi Desert, the dust emissions in the Taklamakan Desert were activated by NLLJs breakdown (Section 3.2). Mid-level westerly winds allowed the eastward export of the dust-laden air from the Taklamakan Desert on 17–18 March (Fig. 9k, l, n, o). The Taklamakan dust reached the West of China, consistent with the relatively lower PM_{10} concentrations in the two eastern cities from 17 March onward (Fig. 11j, l). The wind direction did not allow a further downwind transport of the dust-laden air such that the impact of the dust on the PM_{10} concentrations was limited to the Western cities assessed here (not shown). In short summary, an influence of dust aerosols from the Taklamakan Desert occurred in the west of China, supported by the back-trajectories for specific cities during the dust outbreak (Fig. 12), and the spatial pattern of high PM_{10} concentration and low atmospheric visibility from 17 March onwards (Fig. 5).

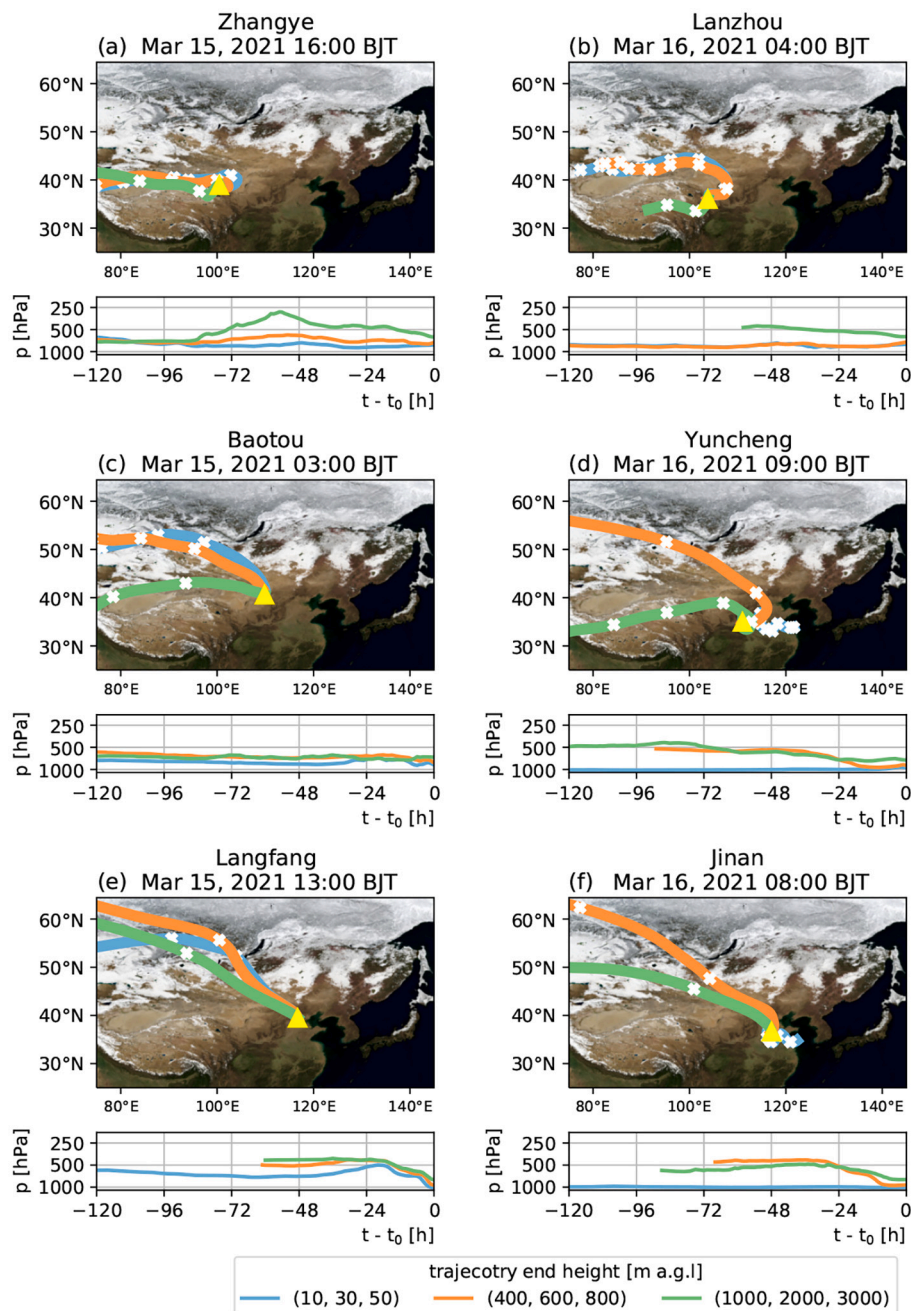


Fig. 12. Mean air mass transport to the cities. Shown are the ensemble-averaged path of the trajectories arriving at different heights above the stations at the time of the maximum PM₁₀. Trajectories in the low, medium and high categories of end points are depicted with blue, orange and green lines. Yellow triangles indicate the station location and white crosses mark 24 h intervals. Back-trajectories are calculated with HYSPLIT using ERA5 data as input. See Section 2 for more information.

4. Conclusion

The present study examined the atmospheric dynamics involved in the development of an unusually strong dust event in mid-March 2021 in China. We investigated the characteristics of the event, dust emission mechanisms in different source regions, and source attribution of dust aerosols in six Chinese cities located in the main dust-affected region. Our conclusions are as follows.

(1) The mid-March 2021 dust event was to some degree surprising in light of the negative trend in low visibility records for March since 2002. The event was driven by a strong Mongolian cyclone caused by a high-temperature gradient, resulting in sea level pressure around 15 hPa lower than the 1st percentile of the March climatology of

1992–2021. Consequently, the dust-emitting winds in the Gobi Desert greatly exceeded the 99th percentile of the 1992–2021 climatology and dust emission thresholds, leading to high levels of dust emissions and southeastward transport along the cold front of the Mongolian cyclone. As a result, the event caused the largest number of stations (48 out of 218) with visibility below 1000m in March since 2002. This outbreak significantly deteriorated air quality across East Asia, as indicated by observations of PM₁₀ concentrations, atmospheric visibility, and the air quality index at the stations.

(2) The passage of the Mongolian cyclone favored the emissions in both the Gobi Desert and the Taklamakan Desert. The arrival of the cold front on 14–15 March 2021 resulted in strong upward winds, which facilitated the upward mixing of dust particles over the Gobi

Desert. The cold air later occupied the Taklamakan Desert on 16 March, leading to the formation of Nocturnal Low-Level Jets (NLLJs). The NLLJ core winds in the early mornings of 16–17 March exceeded the 1992–2021 March climatology by far. The associated strong near-surface winds mobilized dust particles, increasing dust concentrations over the Taklamakan Desert.

(3) The Gobi and Taklamakan Deserts contributed differently to the mid-March 2021 dust storm when measured by the spatial extent of their impacts across East Asia. Dust aerosols from the Gobi Desert were lifted and transported southeastward along the cold front, leading to increased PM concentrations and poor air quality in most Chinese cities. The Taklamakan dust was elevated by deep mixing and transported eastwards by prevailing mid-level westerlies. While the impact of the Taklamakan dust was limited to the western regions of China, it had a significant and profound impact on the air quality of the affected cities.

At the time of writing, another series of spring dust storms affect China with adverse impacts on the urban air quality. The occurrence raises the question whether strong low-pressure system over Mongolia driving high-impact dust outbreaks in East Asia might change in a continuously warming world and to what extent the here newly identified connection between a Mongolian cyclone and the emission of Taklamakan dust aerosols contributes during other events. These topics will be addressed in future research.

CRedit authorship contribution statement

Feifei Mu: Formal-analysis, Investigation, Visualization, Writing-original-draft. **Eduardo Weide Luiz:** Formal-analysis, Investigation, Writing-review-editing. **Stephanie Fiedler:** Conceptualization, Writing-review-editing, Supervision, Funding-acquisition.

Declaration of Competing Interest

The authors declare that they have no known competing financial interests or personal relationships that could have appeared to influence the work reported in this paper.

Data availability

The ground-based atmospheric pollutants data is available through the China Air Quality Online Monitoring and Analysis Platform (<https://www.aqistudy.cn/>). The ground-based meteorological data was obtained from the US National Climatic Data Center (NCDC, <https://www.ncei.noaa.gov/data/global-hourly/access/>). The radiosonde measurements are available through the University of Wyoming (<http://weather.uwyo.edu/upperair/bufrtaob.shtml>). ERA5 reanalysis data was downloaded from the ECMWF Copernicus Climate Data Store (<https://cds.climate.copernicus.eu/>). MERRA-2 reanalysis data was downloaded from the Global Modeling and Assimilation Office of National Aeronautics and Space Administration (https://gmao.gsfc.nasa.gov/reanalysis/MERRA-2/data/_access/). The CAMS forecast data was downloaded from the ECMWF Copernicus Atmosphere Data Store (<https://ads.atmosphere.copernicus.eu/>). The MODIS true color image was obtained from the NASA Worldview (<https://worldview.earthdata.nasa.gov/>).

Acknowledgments

We thank the European Centre for Medium-Range Weather Forecasts for providing ERA5 and CAMS data, the Global Modeling and Assimilation Office of National Aeronautics and Space Administration for providing MERRA-2 reanalysis, the US National Climatic Data Center for providing the ground-based meteorological observations. We further thank the China Air Quality Online Monitoring and Analysis Platform for

acquiring the atmospheric pollutants data and making it available, NASA Worldview for providing the MODIS true color images, and Google Maps for providing access to the topographical map. We thank the University of Wyoming for providing the radiosonde observations. We gratefully acknowledge the NOAA Air Resources Laboratory (ARL) for the provision of the HYSPLIT transport and dispersion model. We thank Leon Knarr for generating and processing the HYSPLIT trajectories, and Mark Meyers for discussions about synoptic-scale dynamics. We thank the two anonymous reviewers and the editor Olivier Dessens for the thoughtful comments and the appraisal of our manuscript.

F. Mu is financially supported by the China Scholarship Council (CSC), grant 202006560002. This work used resources of the Deutsches Klimarechenzentrum (DKRZ) granted by its Scientific Steering Committee (WLA) under project ID bb1198.

References

- Abdi Vishkaee, F., Flamant, C., Cuesta, J., Oolman, L., Flamant, P., Khalesifard, H.R., 2012. Dust transport over Iraq and northwest Iran associated with winter Shamal: A case study. *J. Geophys. Res. Atmos.* 117, D03201. <https://doi.org/10.1029/2011JD016339>.
- Alizadeh-Chooabari, O., Zawar-Reza, P., Sturman, A., 2014. The “wind of 120 days” and dust storm activity over the Sistan basin. *Atmos. Res.* 143, 328–341. <https://doi.org/10.1016/j.atmosres.2014.02.001>.
- An, L., Che, H., Xue, M., Zhang, T., Wang, H., Wang, Y., Zhou, C., Zhao, H., Gui, K., Zheng, Y., Sun, T., Liang, Y., Sun, E., Zhang, H., Zhang, X., 2018. Temporal and spatial variations in sand and dust storm events in East Asia from 2007 to 2016: Relationships with surface conditions and climate change. *Sci. Total Environ.* 633, 452–462. <https://doi.org/10.1016/j.scitotenv.2018.03.068>.
- Bian, H., Tie, X., Cao, J., Ying, Z., Han, S., Xue, Y., 2011. Analysis of a Severe Dust Storm Event over China: Application of the WRF-Dust Model. *Aerosol Air Qual. Res.* 11, 419–428. <https://doi.org/10.4209/aaqr.2011.04.0053>.
- Blackadar, A.K., 1957. Boundary Layer Wind Maxima and Their Significance for the Growth of Nocturnal Inversions. *Bull. Am. Meteorol. Soc.* 38, 283–290. <https://doi.org/10.1175/1520-0477-38.5.283>.
- Bou Karam, D., Flamant, C., Knippertz, P., Reitebuch, O., Pelon, J., Chong, M., Dabas, A., 2008. Dust emissions over the Sahel associated with the West African monsoon intertropical discontinuity region: A representative case-study. *Q. J. R. Meteorol. Soc.* 134, 621–634. <https://doi.org/10.1002/qj.244>.
- Bozzo, A., Benedetti, A., Flemming, J., Kipling, Z., Rémy, S., 2020. An aerosol climatology for global models based on the tropospheric aerosol scheme in the Integrated Forecasting System of ECMWF. *Geosci. Model Dev.* 13, 1007–1034. <https://doi.org/10.5194/gmd-13-1007-2020>.
- Bueh, C., Zhuge, A., Xie, Z., Yong, M., Purejav, G., 2022. The development of a powerful Mongolian cyclone on 14–15 March 2021: Eddy energy analysis. *Atmos. Ocean. Sci. Lett.* 15, 100259. <https://doi.org/10.1016/j.aosl.2022.100259>.
- Chen, S., Huang, J., Li, J., Jia, R., Jiang, N., Kang, L., Ma, X., Xie, T., 2017. Comparison of dust emissions, transport, and deposition between the Taklimakan Desert and Gobi Desert from 2007 to 2011. *Sci. China Earth Sci.* 60, 1338–1355. <https://doi.org/10.1007/s11430-016-9051-0>.
- Chen, S., Zhao, C., Qian, Y., Leung, L.R., Huang, J., Huang, Z., Bi, J., Zhang, W., Shi, J., Yang, L., Li, D., Li, J., 2014. Regional modeling of dust mass balance and radiative forcing over East Asia using WRF-Chem. *Atmos. Res.* 15, 15–30. <https://doi.org/10.1016/j.aeolia.2014.02.001>.
- Cuesta, J., Eremenko, M., Flamant, C., Dufour, G., Laurent, B., Bergametti, G., Höpfer, M., Orphal, J., Zhou, D., 2015. Three-dimensional distribution of a major desert dust outbreak over East Asia in March 2008 derived from IASI satellite observations. *J. Geophys. Res. Atmos.* 120, 7099–7127. <https://doi.org/10.1002/2014JD022406>.
- De Longueville, F., Hountondji, Y.C., Henry, S., Ozer, P., 2010. What do we know about effects of desert dust on air quality and human health in West Africa compared to other regions? *Sci. Total Environ.* 409, 1–8. <https://doi.org/10.1016/j.scitotenv.2010.09.025>.
- Feng, X., Wang, S., 2012. Influence of different weather events on concentrations of particulate matter with different sizes in Lanzhou, China. *J. Environ. Sci.* 24, 665–674. [https://doi.org/10.1016/S1001-0742\(11\)60807-3](https://doi.org/10.1016/S1001-0742(11)60807-3).
- Fiedler, S., Schepanski, K., Heinold, B., Knippertz, P., Tegen, I., 2013. Climatology of nocturnal low-level jets over North Africa and implications for modeling mineral dust emission. *J. Geophys. Res. Atmos.* 118, 6100–6121. <https://doi.org/10.1002/jgrd.50394>.
- Filonchik, M., 2022. Characteristics of the severe March 2021 Gobi Desert dust storm and its impact on air pollution in China. *Chemosphere* 287, 132219. <https://doi.org/10.1016/j.chemosphere.2021.132219>.
- Ge, J.M., Huang, J.P., Xu, C.P., Qi, Y.L., Liu, H.Y., 2014. Characteristics of Taklimakan dust emission and distribution: A satellite and reanalysis field perspective. *J. Geophys. Res. Atmos.* 119, 11772–11783. <https://doi.org/10.1002/2014JD022280>.
- Ge, J.M., Liu, H., Huang, J., Fu, Q., 2016. Taklimakan Desert nocturnal low-level jet: climatology and dust activity. *Atmos. Chem. Phys.* 16, 7773–7783. <https://doi.org/10.5194/acp-16-7773-2016>.

- GMAO, 2015a. MERRA-2 inst33daerNx: 3d,3-Hourly, Instantaneous, Model-Level, Assimilation, Aerosol Mixing Ratio V5.12.4, Greenbelt, MD, USA, Goddard Earth Sciences Data and Information Services Center (GES DISC), Accessed: 1 Jun <https://doi.org/10.5067/LTVB4GPCOTK2>.
- GMAO, 2015b. MERRA-2 tavg12dadgNx: 2d,1-Hourly,Time-averaged,Single-Level, Assimilation, Aerosol Diagnostics (extended) V5.12.4, Greenbelt, MD, USA, Goddard Earth Sciences Data and Information Services Center (GES DISC), Accessed 1 Jun <https://doi.org/10.5067/HM000HQBHKT>.
- GMAO, 2015c. MERRA-2 tavg12daerNx: 2d,1-Hourly, Time-averaged, Single-Level, Assimilation, Aerosol Diagnostics V5.12.4, Greenbelt, MD, USA, Goddard Earth Sciences Data and Information Services Center (GES DISC), Accessed: 1 Jun <https://doi.org/10.5067/KLICLTZ8EM9D>.
- Guan, Q., Cai, A., Wang, F., Yang, L., Xu, C., Liu, Z., 2017. Spatio-temporal variability of particulate matter in the key part of Gansu Province, Western China. *Environ. Pollut.* 230, 189–198. <https://doi.org/10.1016/j.envpol.2017.06.045>.
- Guan, Q., Luo, H., Pan, N., Zhao, R., Yang, L., Yang, Y., Tian, J., 2019. Contribution of dust in northern China to PM10 concentrations over the Hexi corridor. *Sci. Total Environ.* 660, 947–958. <https://doi.org/10.1016/j.scitotenv.2018.12.412>.
- Gui, K., Yao, W., Che, H., An, L., Zheng, Y., Li, L., Zhao, H., Zhang, L., Zhong, J., Wang, Y., Zhang, X., 2022. Record-breaking dust loading during two mega dust storm events over northern China in March 2021: aerosol optical and radiative properties and meteorological drivers. *Atmos. Chem. Phys.* 22, 7905–7932. <https://doi.org/10.5194/acp-22-7905-2022>.
- Hamidianpour, M., Jahanshahi, S.M.A., Kaskaoutis, D.G., Rashki, A., Nastos, P.G., 2021. Climatology of the Sistan Levant wind: Atmospheric dynamics driving its onset, duration and withdrawal. *Atmos. Res.* 260, 105711 <https://doi.org/10.1016/j.atmosres.2021.105711>.
- Hamzeh, N.H., Karami, S., Kaskaoutis, D.G., Tegen, I., Moradi, M., Opp, C., 2021. Atmospheric Dynamics and Numerical Simulations of Six Frontal Dust Storms in the Middle East Region. *Atmosphere* 12 <https://www.mdpi.com/2073-4433/12/1/125>.
- Han, J., Gu, Z., 2021. The Dusty Night of Ulaanbaatar: 2021 East Asia Sandstorm, Trans-Regional Impact, Ecological Imperatives in Mongolia. *Trans-Regional Impact, Ecological Imperatives in Mongolia* (April 9, 2021) <https://dx.doi.org/10.2139/ssrn.3821645>.
- Han, Z., Li, J., Xia, X., Zhang, R., 2012. Investigation of direct radiative effects of aerosols in dust storm season over East Asia with an online coupled regional climate-chemistry-aerosol model. *Atmos. Environ.* 54, 688–699. <https://doi.org/10.1016/j.atmosenv.2012.01.041>.
- Heinold, B., Knippertz, P., Marsham, J.H., Fiedler, S., Dixon, N.S., Schepanski, K., Laurent, B., Tegen, I., 2013. The role of deep convection and nocturnal low-level jets for dust emission in summertime West Africa: Estimates from convection-permitting simulations. *J. Geophys. Res. Atmos.* 118, 4385–4400. <https://doi.org/10.1002/jgrd.50402>.
- Hersbach, H., Bell, B., Berrisford, P., Hirahara, S., Horányi, A., Muñoz-Sabater, J., Nicolas, J., Peubey, C., Radu, R., Schepers, D., Simmons, A., Soci, C., Abdalla, S., Abellan, X., Balsamo, G., Bechtold, P., Biavati, G., Bidlot, J., Bonavita, M., De Chiara, G., Dahlgren, P., Dee, D., Diamantakis, M., Dragani, R., Flemming, J., Forbes, R., Fuentes, M., Geer, A., Haimberger, L., Healy, S., Hogan, R.J., Hólm, E., Janisková, M., Keeley, S., Laloyaux, P., Lopez, P., Lupu, C., Radnoti, G., de Rosnay, P., Rozum, I., Vamborg, F., Villaume, S., Thépaut, J.N., 2020. The ERA5 global reanalysis. *Q. J. Roy. Meteor. Soc.* 146, 1999–2049. <https://doi.org/10.1002/qj.3803>.
- Hu, J., Ying, Q., Wang, Y., Zhang, H., 2015. Characterizing multi-pollutant air pollution in China: Comparison of three air quality indices. *Environ. Int.* 84, 17–25. <https://doi.org/10.1016/j.envint.2015.06.014>.
- Huang, J., Minnis, P., Chen, B., Huang, Z., Liu, Z., Zhao, Q., Yi, Y., Ayers, J.K., 2008. Long-range transport and vertical structure of Asian dust from CALIPSO and surface measurements during PACDEX. *J. Geophys. Res. Atmos.* 113 <https://doi.org/10.1029/2008JD010620>.
- Kaskaoutis, D., Rashki, A., Francois, P., Dumka, U., Houssos, E., Legrand, M., 2015. Meteorological regimes modulating dust outbreaks in southwest Asia: The role of pressure anomaly and Inter-Tropical Convergence Zone on the 1–3 July 2014 case. *Aeolian Res.* 18, 83–97. <https://doi.org/10.1016/j.aeolia.2015.06.006>.
- Kaufman, Y.J., Tanré, D., Boucher, O., 2002. A satellite view of aerosols in the climate system. *Nature* 419, 215–223. <https://doi.org/10.1038/nature01091>.
- Kawai, K., Matsui, H., Tobo, Y., 2021. High Potential of Asian Dust to Act as Ice Nucleating Particles in Mixed-Phase Clouds Simulated With a Global Aerosol-Climate Model. *J. Geophys. Res. Atmos.* 126, e2020JD034263 <https://doi.org/10.1029/2020JD034263>.
- Kim, H., Choi, M., 2015. Impact of soil moisture on dust outbreaks in East Asia: Using satellite and assimilation data. *Geophys. Res. Lett.* 42, 2789–2796. <https://doi.org/10.1002/2015GL063325>.
- Kok, J.F., Adebisi, A.A., Albani, S., Balkanski, Y., Checa-García, R., Chin, M., Colarco, P. R., Hamilton, D.S., Huang, Y., Ito, A., Klose, M., Li, L., Mahowald, N.M., Miller, R.L., Obiso, Y., Pérez García-Pando, C., Rocha-Lima, A., Wan, J.S., 2021. Contribution of the world's main dust source regions to the global cycle of desert dust. *Atmos. Chem. Phys.* 21, 8169–8193. <https://doi.org/10.5194/acp-21-8169-2021>.
- Kurosaki, Y., Mikami, M., 2007. Threshold wind speed for dust emission in east Asia and its seasonal variations. *J. Geophys. Res. Atmos.* 112 <https://doi.org/10.1029/2006JD007988>.
- Li, J., Hao, X., Liao, H., Hu, J., Chen, H., 2021. Meteorological Impact on Winter PM2.5 Pollution in Delhi: Present and Future Projection Under a Warming Climate. *Geophys. Res. Lett.* 48, e2021GL093722 <https://doi.org/10.1029/2021GL093722>.
- Li, J., Hao, X., Liao, H., Yue, X., Li, H., Long, X., Li, N., 2022. Predominant Type of Dust Storms That Influences Air Quality Over Northern China and Future Projections. *Earth's Futur.* 10, e2022EF002649 <https://doi.org/10.1029/2022EF002649>.
- Li, X., Liu, X., Yin, Z.Y., 2018. The Impacts of Taklimakan Dust Events on Chinese Urban Air Quality in 2015. *Atmosphere* 9. <https://doi.org/10.3390/atmos9070281>.
- Ling, X., Guo, W., Fu, C., 2014. Composite analysis of impacts of dust aerosols on surface atmospheric variables and energy budgets in a semiarid region of China. *J. Geophys. Res. Atmos.* 119, 3107–3123. <https://doi.org/10.1002/2013JD020274>.
- Liu, L., Huang, X., Ding, A., Fu, C., 2016. Dust-induced radiative feedbacks in north China: A dust storm episode modeling study using WRF-Chem. *Atmos. Environ.* 129, 43–54. <https://doi.org/10.1016/j.atmosenv.2016.01.019>.
- MEP, 2012. Ambient Air Quality Standards. (Document GB 3095–2012). Ministry of Environmental Protection of the People's Republic of China, Beijing <https://www.mee.gov.cn/ywgz/fgbz/bz/bzwb/dqjhjb/dqjhjb/201203/W020120410330232398521.pdf>.
- Molod, A., Takacs, L., Suarez, M., Bacmeister, J., 2015. Development of the GEOS-5 atmospheric general circulation model: evolution from MERRA to MERRA2. *Geosci. Model. Dev.* 8, 1339–1356. <https://doi.org/10.5194/gmd-8-1339-2015>.
- Pei, L., Yan, Z., Sun, Z., Miao, S., Yao, Y., 2018. Increasing persistent haze in Beijing: potential impacts of weakening East Asian winter monsoons associated with northwestern Pacific sea surface temperature trends. *Atmos. Chem. Phys.* 18, 3173–3183. <https://doi.org/10.5194/acp-18-3173-2018>.
- QGIS Development Team, 2022. QGIS Geographic Information System. QGIS Association <https://www.qgis.org>.
- Qian, W., Leung, J.C.H., Ren, J., Du, J., Feng, Y., Zhang, B., 2022. Anomaly Based Synoptic Analysis and Model Prediction of Six Dust Storms Moving From Mongolia to Northern China in Spring 2021. *J. Geophys. Res. Atmos.* 127, e2021JD036272 <https://doi.org/10.1029/2021JD036272>.
- Rashki, A., Kaskaoutis, D., Mofidi, A., Minvielle, F., Chiappello, I., Legrand, M., Dumka, U., Francois, P., 2019. Effects of Monsoon, Shamal and Levant winds on dust accumulation over the Arabian Sea during summer – The July 2016 case. *Aeolian Res.* 36, 27–44. <https://doi.org/10.1016/j.aeolia.2018.11.002>.
- Rashki, A., Kaskaoutis, D., Rautenbach, C., Eriksson, P., Qiang, M., Gupta, P., 2012. Dust storms and their horizontal dust loading in the Sistan region, Iran. *Aeolian Res.* 5, 51–62. <https://doi.org/10.1016/j.aeolia.2011.12.001>.
- Rolph, G., Stein, A., Stunder, B., 2017. Real-time Environmental Applications and Display sYstem: READY. *Environ. Modell. Software* 95, 210–228. <https://doi.org/10.1016/j.envsoft.2017.06.025>.
- Sandstrom, T., Forsberg, B., 2008. Desert dust: an unrecognized source of dangerous air pollution? *Epidemiology* 19, 808–809. <https://doi.org/10.1097/EDE.0b013e31818809e0>.
- Schweitzer, M.D., Calzadilla, A.S., Salamo, O., Sharifi, A., Kumar, N., Holt, G., Campos, M., Mirsaeidi, M., 2018. Lung health in era of climate change and dust storms. *Environ. Res.* 163, 36–42. <https://doi.org/10.1016/j.envres.2018.02.001>.
- Shao, Y., Dong, C., 2006. A review on east asian dust storm climate, modelling and monitoring. *Glob. Planet. Change* 52, 1–22. <https://doi.org/10.1016/j.gloplacha.2006.02.011>.
- Shao, Y., Lu, H., 2000. A simple expression for wind erosion threshold friction velocity. *J. Geophys. Res. Atmos.* 105, 22437–22443. <https://doi.org/10.1029/2000JD900304>.
- Song, H., Zhang, K., Piao, S., Wan, S., 2016. Spatial and temporal variations of spring dust emissions in northern China over the last 30 years. *Atmos. Environ.* 126, 117–127. <https://doi.org/10.1016/j.atmosenv.2015.11.052>.
- Song, Q., Zhang, Z., Yu, H., Kato, S., Yang, P., Colarco, P., Remer, L.A., Ryder, C.L., 2018. Net radiative effects of dust in the tropical North Atlantic based on integrated satellite observations and in situ measurements. *Atmos. Chem. Phys.* 18, 11303–11322. <https://doi.org/10.5194/acp-18-11303-2018>.
- Stein, A.F., Draxler, R.R., Rolph, G.D., Stunder, B.J.B., Cohen, M.D., Ngan, F., 2015. NOAA's HYSPLIT Atmospheric Transport and Dispersion Modeling System. *B. Am. Meteorol. Soc.* 96, 2059–2077. <https://doi.org/10.1175/BAMS-D-14-00110.1>.
- Takemi, T., Seino, N., 2005. Dust storms and cyclone tracks over the arid regions in east Asia in spring. *J. Geophys. Res. Atmos.* 110 <https://doi.org/10.1029/2004JD004698>.
- Takemura, T., Uno, I., Nakajima, T., Higurashi, A., Sano, I., 2002. Modeling study of long-range transport of Asian dust and anthropogenic aerosols from East Asia. *Geophys. Res. Lett.* 29, 11-1–11-4. <https://doi.org/10.1029/2002GL016251>.
- Tao, M., Chen, L., Wang, J., Wang, L., Wang, W., Lin, C., Gui, L., Wang, L., Yu, C., Wang, Y., 2022. Characterization of dust activation and their prevailing transport over East Asia based on multi-satellite observations. *Atmos. Res.* 265, 105886 <https://doi.org/10.1016/j.atmosres.2021.105886>.
- Tian, Y., Pan, X., Wang, Z., Wang, D., Ge, B., Liu, X., Zhang, Y., Liu, H., Lei, S., Yang, T., Fu, P., Sun, Y., Wang, Z., 2020. Transport Patterns, Size Distributions, and Depolarization Characteristics of Dust Particles in East Asia in Spring 2018. *J. Geophys. Res. Atmos.* 125, e2019JD031752 <https://doi.org/10.1029/2019JD031752>.
- Vogel, A., Alessa, G., Scheele, R., Weber, L., Dubovik, O., North, P., Fiedler, S., 2022. Uncertainty in Aerosol Optical Depth From Modern Aerosol-Climate Models, Reanalyses, and Satellite Products. *J. Geophys. Res. Atmos.* 127, e2021JD035483 <https://doi.org/10.1029/2021JD035483>.
- Wang, H., Jia, X., Li, K., Li, Y., 2015. Horizontal wind erosion flux and potential dust emission in arid and semiarid regions of China: A major source area for East Asia dust storms. *CATENA* 133, 373–384. <https://doi.org/10.1016/j.catena.2015.06.011>.
- Wang, Q., Gu, J., Wang, X., 2020. The impact of Sahara dust on air quality and public health in European countries. *Atmos. Environ.* 241, 117771 <https://doi.org/10.1016/j.atmosenv.2020.117771>.
- Wang, Y., Wang, R., Ming, J., Liu, G., Chen, T., Liu, X., Liu, H., Zhen, Y., Cheng, G., 2016. Effects of dust storm events on weekly clinic visits related to pulmonary tuberculosis disease in Minqin. *China. Atmos. Environ.* 127, 205–212. <https://doi.org/10.1016/j.atmosenv.2015.12.041>.

- Van de Wiel, B.J., Moene, A., Steeneveld, G., Baas, P., Bosveld, F., Holtslag, A., 2010. A Conceptual View on Inertial Oscillations and Nocturnal Low-Level Jets. *J. Atmos. Sci.* 67, 2679–2689. <https://doi.org/10.1175/2010JAS3289.1>.
- Wu, C., Lin, Z., Shao, Y., Liu, X., Li, Y., 2022. Drivers of recent decline in dust activity over East Asia. *Nat. Commun.* 13, 7105. <https://doi.org/10.1038/s41467-022-34823-3>.
- Yu, Y., Kalashnikova, O.V., Garay, M.J., Notaro, M., 2019. Climatology of Asian dust activation and transport potential based on MISR satellite observations and trajectory analysis. *Atmos. Chem. Phys.* 19, 363–378. <https://doi.org/10.5194/acp-19-363-2019>.
- Yuan, T., Chen, S., Huang, J., Wu, D., Lu, H., Zhang, G., Ma, X., Chen, Z., Luo, Y., Ma, X., 2019. Influence of Dynamic and Thermal Forcing on the Meridional Transport of Taklimakan Desert Dust in Spring and Summer. *J. Clim.* 32, 749–767. <https://doi.org/10.1175/JCLI-D-18-0361.1>.
- Zhang, L., Cao, X., Bao, J., Zhou, B., Huang, J., Shi, J., Bi, J., 2010. A case study of dust aerosol radiative properties over Lanzhou, China. *Atmos. Chem. Phys.* 10, 4283–4293 <https://acp.copernicus.org/articles/10/4283/2010/>.
- Zhang, X., Sharratt, B., Liu, L., Wang, Z., Pan, X., Lei, J., Wu, S., Huang, S., Guo, Y., Li, J., et al., 2018. East Asian dust storm in May 2017: observations, modelling, and its influence on the Asia-Pacific region. *Atmos. Chem. Phys.* 18, 8353–8371. <https://doi.org/10.5194/acp-18-8353-2018>.
- Zhang, Z., Zhou, W., Wenig, M., Yang, L., 2017. Impact of long-range desert dust transport on coastal East Asia: analysis of urban dust concentration and wet deposition with model simulation. *Air Qual. Atmos. Hlth.* 10, 325–337. <https://doi.org/10.1007/s11869-016-0440-1>.
- Zhao, A., Ryder, C.L., Wilcox, L.J., 2022. How well do the CMIP6 models simulate dust aerosols? *Atmos. Chem. Phys.* 22, 2095–2119. <https://doi.org/10.5194/acp-22-2095-2022>.
- Zhao, S., Yu, Y., Xia, D., Yin, D., He, J., Liu, N., Li, F., 2015. Urban particle size distributions during two contrasting dust events originating from Taklimakan and Gobi Deserts. *Environ. Pollut.* 207, 107–122. <https://doi.org/10.1016/j.envpol.2015.08.052>.